Radial 1-D seismic structures in the deep mantle in mantle convection simulations with self-consistently calculated mineralogy

Takashi Nakagawa
Institute for Research on Earth Evolution, Japan Agency for Marine–Earth Science and Technology, 236-0001 Yokohama, Japan (ntakashi@jamstec.go.jp)

Paul J. Tackley
Institute of Geophysics, Department of Earth Sciences, ETH Zurich, CH-8092 Zurich, Switzerland

Frédéric Deschamps
Institute of Earth Sciences, Academia Sinica, Taipei 115, Taiwan

James A. D. Connolly
Institute of Geochemistry and Petrology, Department of Earth Sciences, ETH Zurich, CH–8092 Zurich, Switzerland

[1] Numerical thermo-chemical mantle convection simulations in a spherical annulus geometry with self-consistently calculated mineralogy and mineral physics are used to predict detailed deep mantle seismic structures, particularly local radial profiles of shear wave velocity (Vs) and bulk sound velocity (Vb). The predicted structures are compared to seismological observations and used to guide the interpretation of seismic observations and to test the model. The mantle composition is described as a mixture of MORB (Mid-Oceanic-Ridge-Basalt) and harzburgitic end-members in the Na_2O-CaO-FeO-MgO-Al_2O_3-SiO_2 system. To assess the influence of chemical variability, four different sets of end-member compositions are evaluated. Results confirm that the post-perovskite (pPv) phase causes anti-correlated S wave and bulk sound velocities in the deep mantle, due to pPv being fast in Vs but slow in bulk sound velocity. Local 1-D seismic profiles display great lateral variability, and often have multiple discontinuities in the deep mantle due to MORB layers in folded slabs, with a positive Vs anomaly and negative bulk sound anomaly, or the perovskite-pPv phase transition. The pPv transition is not visible inside piles of segregated MORB because of the high temperature and small velocity contrast of pPv in MORB. Piles of segregated MORB are seismically slow in both Vs and bulk sound despite being expected to be fast in Vs, because they are hotter than the surrounding material. Anelasticity has a significant influence on profiles of Vs only in the lower thermal boundary layer, which corresponds to below 2600 to 2800 km depth depending on region, where temperatures are higher than the extrapolated adiabat. These results indicate the importance of using a joint geodynamical-mineralogical approach to predict and aid in the interpretation of deep mantle seismic structure, because interpretations based on seismology and mineral physics alone may be misleading and do not capture the strong lateral variability in 1-D structure obtained here: for example, multiple reflections arising from folded slabs and the precise balance between thermal and compositional influences on seismic structure.

1. Introduction

[2] Seismic analyses indicate that the Earth's lowermost mantle is characterized by substantial thermal, chemical and mineralogical complexity due to the presence of a thermal boundary layer and the likely presence of piles of dense material and the post-perovskite phase (for reviews see, e.g., *Garnero and McNamara* [2008] and *Tackley* [2012]). Waveform analyses that search for reflections in the deep mantle suggest a double phase transformation: from perovskite to post-perovskite then the reverse transition back to perovskite [*Thomas et al.*, 2004; *Hernlund et al.*, 2005; *Lay et al.*, 2006; *Avants et al.*, 2006; *van der Hilst et al.*, 2007; *Kawai et al.*, 2007, 2009; *Sun and Helmberger*, 2008]. Many of these studies also found strong lateral variations in the seismic profiles, with *Hutko et al.* [2006] finding a step in the seismic discontinuity that they interpreted as due to a folded slab, while *Konishi et al.* [2009] found evidence for the presence of MORB. The shear wave velocity of the post-perovskite phase is several percent faster than that of perovskite [*Tsuchiya et al.*, 2004]. On the other hand, the compressional (P) wave or bulk sound velocity of post-perovskite is thought to be ~0.5 to 1.5% slower than $MgSiO_3$ [*Wookey et al.*, 2005; *Shim et al.*, 2008]. The combination of these can cause an anticorrelation in seismic velocities [*Wookey et al.*, 2005; *Hutko et al.*, 2008].

[3] A series of numerical mantle convection simulations with melting-induced chemical differentiation, multiple phase transitions, plate tectonics-like lithospheric behavior and compressibility have suggested that large-scale seismic heterogeneity in the deep mantle can be explained by the post-perovskite phase causing fast Vs anomalies and hot basaltic material segregated from subducted slabs causing slower Vs anomalies [*Nakagawa and Tackley*, 2005, 2006]. These studies used a simple linear scaling to convert thermal and compositional structure to seismic anomalies, and did not study radial one-dimensional (1-D) profiles that could be compared to seismic analyses. In more recent simulations [*Nakagawa et al.*, 2009, 2010], the computation of physical properties by free energy minimization has been used to provide a self-consistent model for mantle mineralogy and seismic velocity structure. These studies found important differences in seismic structure, but addressed only large-scale spectral features of S-wave heterogeneity. Here we extend our mantle convection simulations to investigate and characterize local one-dimensional (1-D) radial profiles of S-wave and bulk sound velocities and relate these to interpretations of seismic waveform analyses, with particular emphasis on the potential role of post-perovskite in the lowermost mantle.

2. Model Description

2.1. Mineralogical Modeling

[4] We assume that the average mantle composition is pyrolitic [*Ringwood*, 1985] and that, at any point in the mantle, the local composition can be expressed in terms of the compositions of a basaltic and a harzburgitic end-member. Local physical properties, including mineralogy and elastic moduli, are taken to be the average of the corresponding properties in the end-member lithologies (i.e., the mechanical mixture model of *Xu et al.* [2008]), which are computed as a function of pressure and temperature by free-energy minimization. These properties, which are summarized in look-up tables, are used in the convection model and during post-processing to compute seismic wave speeds. Our formulation of the energy equation [*Nakagawa et al.*, 2009] does not include explicit terms to account for the latent heat and volumetric effects associated with the continuous chemical requilibration of the end-member lithologies as a function of pressure and temperature. Accordingly, we account for these effects implicitly by using effective expansivity and heat capacity,

Table 1. Bulk Compositions of MORB and Harzburgite in Molar Percent, and Pyrolite Taken From *Ringwood* [1985][a]

	NCFMAS-R		NCFMAS-H		NCFMAS-I		NCFMAS-O		
	harz	MORB	harz	MORB	harz	MORB	harz	MORB	Pyrolite
CaO	1.65	11.74	0.61	13.05	1.94	10.55	1.53	11.20	3.4
FeO	6.55	9.73	6.36	7.68	6.42	11.43	6.35	9.90	8.0
MgO	37.54	8.46	36.56	10.49	37.63	8.51	37.52	7.70	38.8
Al_2O_3	2.04	15.89	0.96	16.08	2.35	14.88	1.78	15.70	4.4
SiO_2	37.60	49.74	34.22	50.39	37.97	51.00	36.50	51.00	45.0
Na_2O	N/A	2.69	N/A	1.87	N/A	2.90	N/A	2.4	0.4

[a]To generate harzburgite compositions, the fraction of MORB extracted from pyrolite is 0.15 for NCFMAS-R, 0.21 for NCFMAS-H, 0.14 for NCFMAS-I and 0.17 for NCFMAS-O.

which are computed by finite differences from the properties summarized in our look-up tables as

$$C_{P,eff} = \left(\frac{\partial H}{\partial T} \right)_P; \quad \alpha_{eff} = -\frac{1}{\rho} \frac{\partial \rho}{\partial T} \qquad (1)$$

where H is enthalpy, T is temperature, P is pressure and ρ is density. This effective thermal expansivity is never used to calculate thermal expansion because density comes directly from look-up tables. The look-up tables used for the modeling presented here have temperature and pressure resolution of, respectively, 5 K and ~45 MPa (actually 1 km in depth).

[5] The compositions of the end-member lithologies are defined in terms of the six most abundant oxides in Earth's mantle, Na_2O-CaO-FeO-MgO-Al_2O_3-SiO_2, hereafter abbreviated as NCFMAS. Due to the uncertainty and natural variation in MORB composition, we test four different MORB compositions, namely NCFMAS-R [*Ricolleau et al.*, 2010], NCFMAS-H [*Hirose et al.*, 2005], NCFMAS-I [*Irifune and Ringwood*, 1993] and NCFMAS-O [*Ono et al.*, 2005]. For each of these four MORB compositions, we calculate four complementary harzburgite compositions by extracting the maximum amount of MORB from pyrolite. The fraction of MORB that can be extracted ranges from 0.14 to 0.21. Table 1 shows the compositions in oxides for pyrolite and the four compositional models we consider. All physical properties including elastic properties were calculated using Perple_X [*Connolly*, 2005, 2009] with the mineral properties database from *Stixrude and Lithgow-Bertelloni* [2011]. For the $MgSiO_3$ system, the data of *Stixrude and Lithgow-Bertelloni* [2011] fits the experimental constraints of *Tateno et al.* [2009] and is therefore broadly consistent with the Clapeyron slope of 13.3 ± 1 MPa/K inferred by *Tateno et al.* [2009]. In comparison to the databases used in our earlier models (*Nakagawa et al.* [2010] used the data from *Xu et al.* [2008]), the *Stixrude and Lithgow-Bertelloni* [2011] database

takes into account new constraints on the properties of Al- and Fe- perovskite and should therefore provide a more accurate model for the Pv-pPv phase transition. Figure 1 shows the calculated density difference between each of the MORB compositions and the corresponding harzburgite and pyrolite compositions, as a function of temperature and pressure. The intervals of depth and temperature used in these plots are the numerical grid spacing in the radial direction and 20 K for temperature. In order that the effect of sharp phase boundaries on physical properties are correctly represented, look-up tables have a much finer resolution of 1 km in the depth direction by 5 K in temperature and physical properties are block-averaged to the resolution actually used. Apart from the complex phase transitions in the transition zone region, which include a MORB density crossover below 660 km for relatively high temperatures, the perovskite to post-perovskite transition is visible as an upward-sloping line that intersects the CMB at around 3800 K. Density profiles for all four compositional models are shown in Figure 2, which indicates that post-perovskite has a strong influence on the density of harzburgite but a relatively small effect on the density of basalt. It also shows significant differences in the MORB-harzburgite density difference between different compositional models.

[6] Previous studies suggested that anelastic effects may be important in the mantle and should be accounted for when calculating seismic velocity from temperature and pressure [e.g., *Goes et al.*, 2000; *Matas and Bukowinski*, 2007]. Other studies pointed out that the velocity changes induced by anelasticity are moderate and remain within the error bars induced by the uncertainties on the thermoelastic properties of mantle minerals [*Trampert et al.*, 2001; *Brodholt et al.*, 2007; *Khan et al.*, 2011]. It was also pointed out that due to high pressure, anelastic effects may be limited in the lowermost mantle.
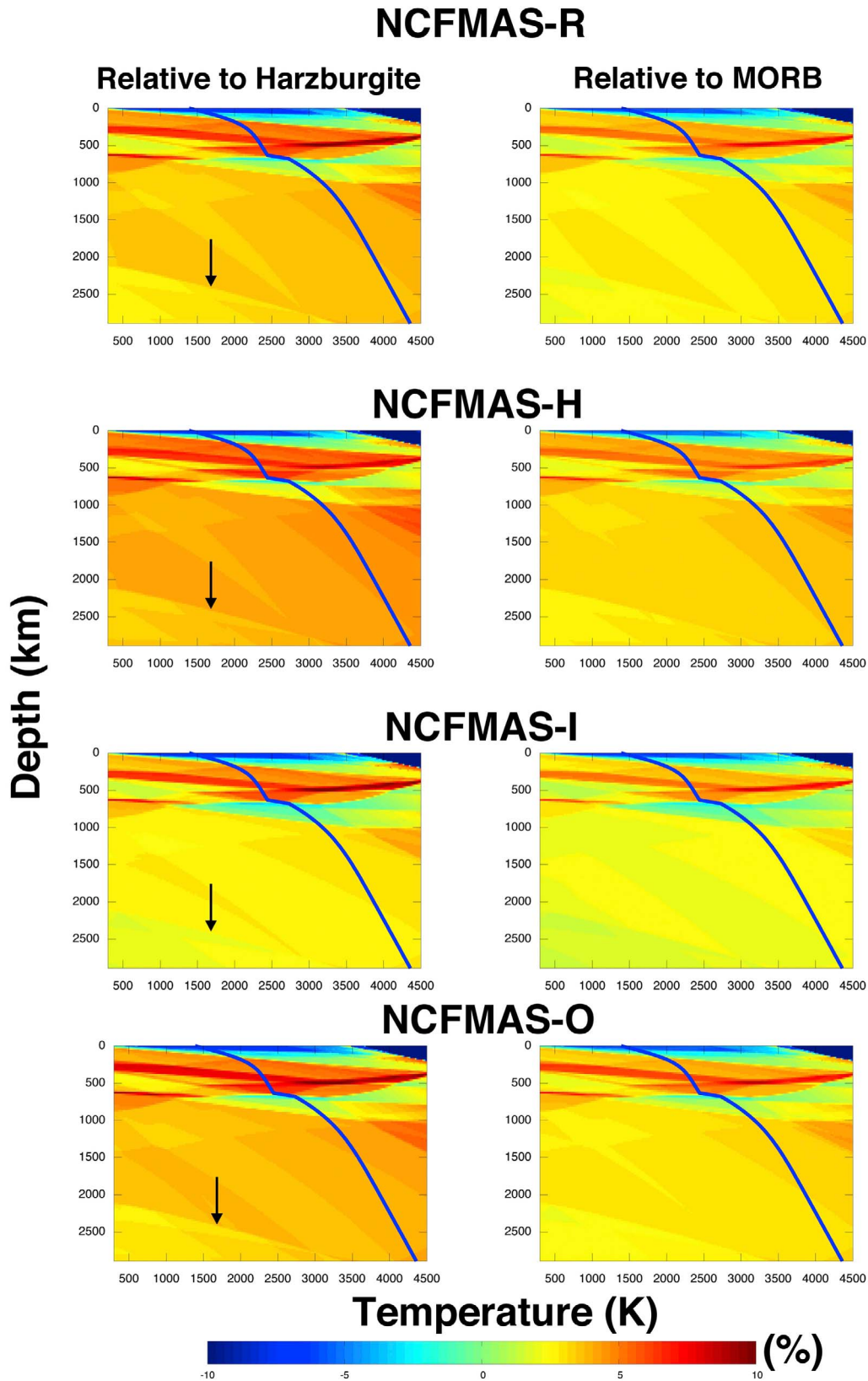
Figure 1. Density difference of MORB relative to harzburgite and pyrolite as a function of depth and temperature for all four compositional models. Arrows indicate the phase boundary between perovskite and post-perovskite.
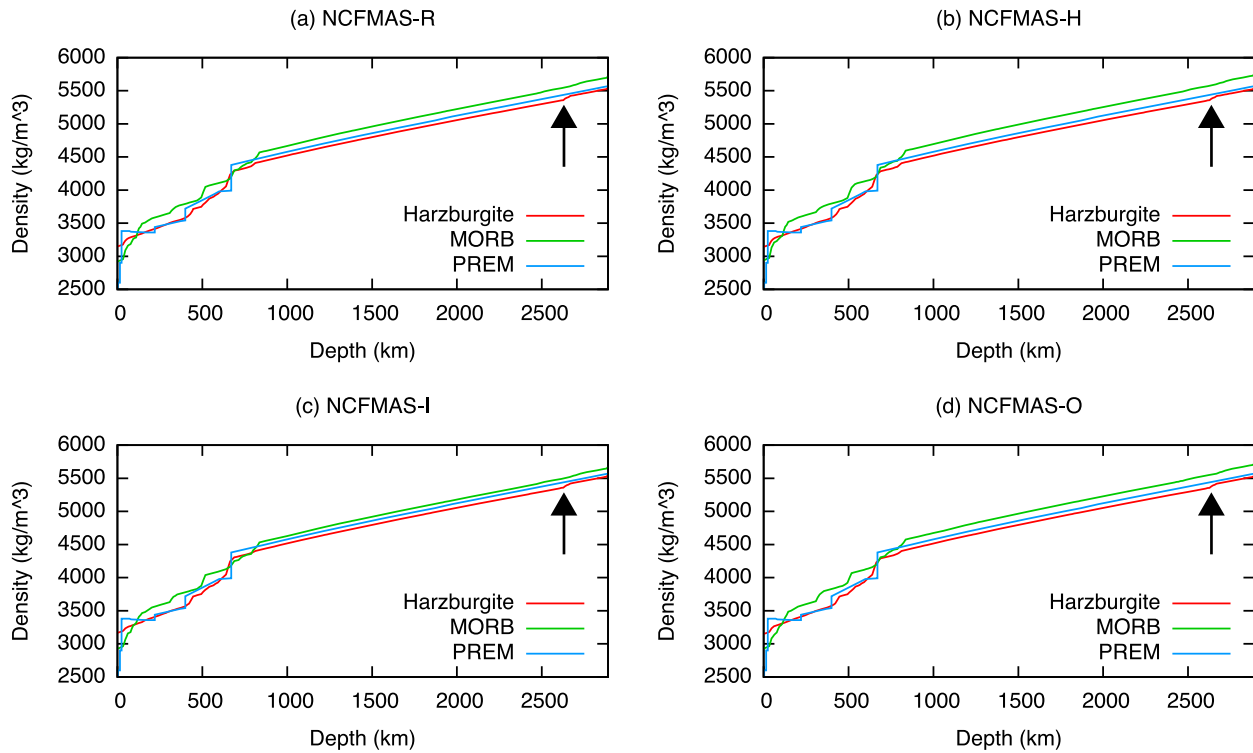
Figure 2. Density profiles for the different compositions along an adiabat with 1600 K potential temperature, together with the PREM [*Dziewonski and Anderson*, 1981] density profile. Arrows show the position of boundary between perovskite and post-perovskite phase transition detected from Figure 1.

However, in locations where temperature is very high, anelasticity may be important even in the lowermost mantle. Here we incorporate temperature- and depth-dependent anelasticity into seismic velocity calculations following

$$V_s(T,P,\omega) = V_s^{el}\left[1 - \frac{1}{2}\cot\left(\frac{\alpha\pi}{2}\right)Q_s^{-1}(T,P,\omega)\right]$$
$$Q_s(T,P,\omega) = \omega^2 Q_0 \exp\left[\alpha\frac{(E+PV)}{RT}\right] \qquad (2)$$

where V_s^{el} is the elastic shear velocity (here calculated using Perple_X), Q_s the quality factor for S-wave velocity, Q_0 a prefactor for the quality factor, ω the frequency of seismic waves fixed at 1 Hz, α is the frequency exponent ($0 < \alpha < 1$), R is the gas constant, and E and V are the activation energy and volume for anelasticity.

[7] The above equations for Vs and Q are well-established, thus the main difference between anelasticity models is in the choice of α and activation enthalpy (H*(r), which is written as E + PV above); in any case parameters should be chosen such that Q(r) is within the range obtained from inversions of seismic data (see *Matas and Bukowinski* [2007] for a comparison of Q models). Here we briefly review the plausible range of these parameters. *Matas and*

Bukowinski [2007] choose α = 0.3 and gave 'minimum' and 'maximum' end-members for H*(r), which over the lower mantle increase from 250 to 340 kJ/mol or 620–850 kJ/mol, respectively. *Brodholt et al.* [2007] varied α from 0.1 to 0.4 and H* from 200 to 700 kJ/mol, calculating what effect these variations have on dlnVs/dlnVp. *Goes et al.* [2004] chose α = 0.15 and H* increasing from 204 to 333 kJ/mol (Model Q4), or 408–665 kJ/mol (Model Q6) (although the equation for Q(T) in *Goes et al.* [2004] did not include α inside the exponential, it was included in their actual calculation).

[8] Here we choose α = 0.3, E = 300 kJ/mol and V = 1.5 cm³/mol, giving H* that increases from 337 to 504 kJ/mol over the lower mantle, which is roughly in the middle of the ranges given in the above studies. Q_0 is calculated such that Q on the adiabat at the top of the lower mantle is 300, which is in the range of what is seismically observed (see Figure 2 of *Matas and Bukowinski* [2007] for a plot of the various seismic models).

2.2. Mantle Convection Simulations

[9] For details of the numerical mantle convection simulations with self-consistently calculated mineral physics the reader is referred to our previous

studies [*Nakagawa et al.*, 2009, 2010]. Here, only the main features and differences from our previous studies are described. A 2-D spherical annulus [*Hernlund and Tackley*, 2008] rather than a full 3-D spherical shell is used to facilitate higher resolution and convective vigor as well as allow the full solution and related radial profiles to be visualized in a straightforward manner. Compressibility is included using the truncated anelastic approximation, giving a standard set of equations for conservation of mass, momentum and energy that we here reproduce for completeness in dimensional form:

$$\nabla \cdot \left(\rho \underline{v}\right) = 0; \nabla \cdot \underline{\sigma} - \nabla p = \rho g;$$

$$\underline{\sigma} = \eta \left(\nabla \underline{v} + \left(\nabla \underline{v}\right)^T - \frac{2}{3}\nabla \cdot \underline{v}\right) \quad (3)$$

$$\rho C_p \frac{DT}{Dt} = \nabla \cdot (k\nabla T) + \rho H - \alpha \rho g v_r T + \underline{\sigma} : \underline{\dot{e}}$$

where ρ = density of pyrolite composition, v = velocity and v_r its radial component, σ = stress, p = pressure, g = gravity, C_p = effective heat capacity, T = absolute temperature, t = time, k = thermal conductivity, H = radiogenic heating rate, α = effective thermal expansivity and $\dot{e}$ = strain rate. Density, effective heat capacity and effective thermal expansivity are taken from lookup tables calculated using Perple_X. Density as a function of temperature, depth and composition (i.e., for a mixture of harzburgite and MORB endmembers) is given by

$$\rho(T,z,C) = (1-C)\rho_{hz}(T,z) + C\rho_{MORB}(T,z) \quad (4)$$

where $\rho_{hz}(T, z)$ = density of harzburgite and $\rho_{MORB}(T, z)$ = density of MORB, which are both calculated as the inverse of specific volume calculated by Perple_X (which calculates this using the Mie-Gruneisen formulation of *Stixrude and Lithgow-Bertelloni* [2005]), and C is the MORB fraction. H and g are taken to be constant (see Table 1), k is depth-dependent with a power law dependence on density [*Nakagawa et al.*, 2009], and velocity, pressure, temperature, stress, and strain rate are solved for. Viscosity, which enters into the stress tensor, is dependent on temperature, depth and yield stress, given by

$$\eta_m\left(\tilde{T},\tilde{d}\right) = A_0 \exp\left[9.1535\tilde{d}\right] \exp\left[\frac{32.716}{\tilde{T}+0.88}\right]$$

$$\eta_Y = \frac{\sigma_0 + \sigma_1 \tilde{d}}{2\dot{e}} \quad (5)$$

$$\eta = \left(\frac{1}{\eta_m} + \frac{1}{\eta_Y}\right)^{-1}$$

where tildes denote nondimensional quantities T is nondimensionalized to 2500 K and d to mantle depth) and A_0 is a prefactor determined such that η_m(T = 1600 K, d = 0) = η_{ref}, σ_0 and σ_1 are yield stress at the surface and yield stress gradient, and $\dot{e}$ is the 2nd invariant of the strain rate tensor. Values are given in Table 1.

[10] In some cases, oceanic crust and complementary depleted material are produced by partial melting of the mantle when it reaches a depth-dependent solidus, with the amount of melting calculated such that the temperature stays on the solidus. A difference compared to our previous studies is that the CMB temperature and internal heating rate are fixed in time. The model parameters used here, which are different from our previous paper [*Nakagawa et al.*, 2010], are listed in Table 2. Density, heat capacity and thermal expansivity are not listed in this table because they come from the Perple_X calculated tables. The numerical resolution used here is 1024 × 128 cells with radial grid refinement to resolve the CMB region at 10 km radial resolution, and 30 tracers per cell (a total of 4 million) to track the composition and melt fraction. In a 3D spherical shell this would require 50 million grid points and 1.5 billion tracers, which is now feasible but would take considerably more resources to run. Tests of resolution are presented in section A1.

3. Results

[11] Here we show results for two series of simulations: isochemical and thermo-chemical (with the generation of oceanic crust by partial melting). Eight cases are presented. For isochemical cases, we assume that pyrolite is a mechanical mixture of harzburgite and MORB [*Xu et al.*, 2008]. Because of this mechanical mixture, the physical properties are slightly different for each compositional model, even with the same bulk composition. For thermo-chemical cases, in which melting-induced differentiation creates oceanic crust, the initial compositional field is uniform with the same mechanical mixture as in the isochemical cases. The surface velocity is around 10 cm/yr for isochemical cases and 5 cm/yr for thermo-chemical cases and conductive surface heat flow is around 46 TW for isochemical cases and 23 TW for thermochemical cases.

3.1. Isochemical Cases

[12] Figure 3 shows temperature and seismic anomalies of shear wave (Vs) and bulk sound (Vb)

Table 2. Mantle Model Parameters

Symbol	Meaning	Value
η_0	Reference viscosity	1.4×10^{21} Pa s
σ_b	Yield stress at surface	50 MPa
σ_d	Yield stress gradient	39 Pa m^{-1}
T_s	Surface Temperature	300 K
T_{CMB}	CMB Temperature	3850 K
H	Internal heating rate	3.7×10^{-12} W/kg
g	Gravitational acceleration	9.81 m/s^2

velocity for the isochemical case with NCFMAS-I at t = 4.5 Gyrs from the initial condition. Seismic anomalies plotted here are relative to the 1-D azimuthally averaged profile of calculated Vs or Vb structure, rather than relative to some seismic model. Small-scale plumes rising from the CMB region are found, which is consistent with the dynamical feature associated with the post-perovskite phase in compressible mantle convection simulations with a much simpler rheology than assumed here [*Nakagawa and Tackley*, 2004]. Thin patches of post-perovskite are present above the CMB. In these patches, which are colder than average mantle, Vs is faster than average and Vb is slower than average, therefore resulting in an anticorrelation between Vs and Vb, consistent with the seismic signature of the post-perovskite phase predicted from mineral physics theory [*Wookey et al.*, 2005]. The seismic anomalies shown here do not include the effects of anelasticity, which is analyzed later.
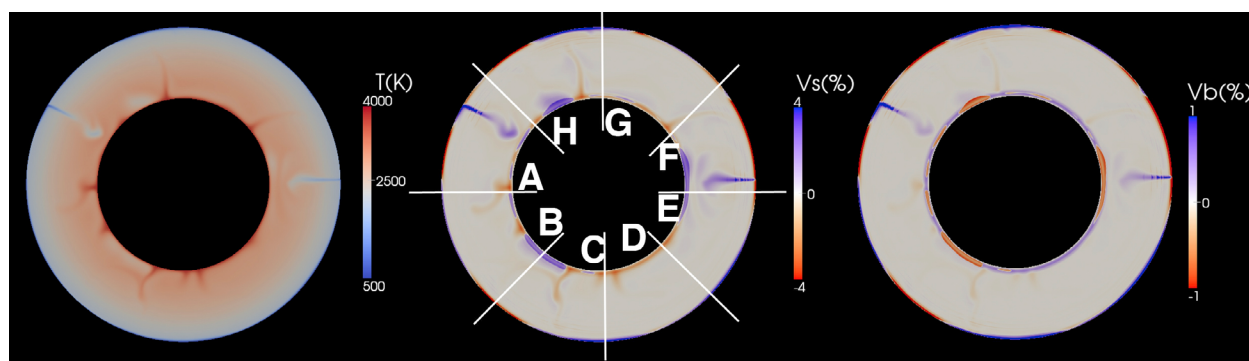
[13] Temporal variations of the temperature field for NCFMAS-I are shown in Figure 4. The general character of the solution, with small-scale plumes enhanced by the post-perovskite phase transition and one to two downwelling slabs, is already established by t = 1.1 Gyrs and continues to t = 3 Gyrs and 4.6 Gyrs. This indicates that the snapshot of thermal

structure shown in Figure 3 is reliable for inferring the general character of seismic structures calculated from the thermal structure.

[14] Temperature and seismic anomalies for isochemical cases with other compositional models are shown in Figure 5. The general character of the features is similar to those in Figure 3, which means that small-scale structure near the CMB caused by post-perovskite effects is consistent with our previous numerical mantle convection simulations that did not use self-consistently calculated mineralogy [*Nakagawa and Tackley*, 2004].

3.2. Thermochemical Cases

[15] Figure 6 shows temperature, composition and seismic anomalies (S-wave and bulk sound velocity) at t = 4.5 Gyrs from the initial condition for NCFMAS-I. Cold subducted slabs are strongly deformed in the lowermost mantle, often forming folded structures above the CMB. Weak and large-scale upwelling plumes are also observed in the thermal structure. Basaltic crust segregates from subducted slabs above the core-mantle boundary (CMB) then forms large-scale compositionally distinct piles, which have a heterogeneous internal structure. Outside the piles, blobs and strips of basalt are also visible. Such general structures were also observed in our previous studies [*Nakagawa et al.*, 2009, 2010] and are also consistent with *Brandenburg et al.* [2008] which uses force-balanced plates; one difference is that our results include strongly bending and folding slabs in the deep mantle. Additional features noted here are upwelling plumes rising from the edge of the basaltic piles or between pooled cold slabs. Because the basaltic piles are relatively hot, they are seismically slow in Vs despite the fact that basalt is intrinsically (i.e., at the same temperature and pressure) faster than

Figure 3. (left) Temperature, (middle) shear wave and (right) bulk sound velocity anomalies for isochemical model of NCFMAS-I at 4.5 Gyrs. Section lines indicate 1-D structures shown in Figure 9.

Figure 4. Temporal variation of temperature field for an isochemical cases of NCFMAS-I.

pyrolite or harzburgite [*Xu et al.*, 2008]. This is broadly consistent with the observation that LLSVPs (large low shear velocity provinces) correspond to regions where the shear wave velocity is slower than average [e.g., *Trampert et al.*, 2004; *Simmons et al.*, 2010; *Ritsema et al.*, 2011; *Mosca et al.*, 2012]. In the perovskite stability field basaltic piles are also slow in Vb but by a much smaller percentage. In contrast, basalt in cold regions, such as in slabs reaching the CMB region, is seismically fast in Vs but slow in Vb. In the lowest ∼300 km, patches of post-perovskite are visible in cold regions [*Nakagawa and Tackley*, 2005], being seismically fast in Vs but slow in Vb. Again, this is consistent with high pressure mineral physics [*Tsuchiya et al.*, 2004; *Wookey et al.*, 2005; *Shim et al.*, 2008] as well as seismic observations [*Wookey et al.*, 2005; *Hutko et al.*, 2008]. For Vs, post-perovskite thus increases the velocity contrast between piles and the cold regions between piles, whereas, for bulk sound anomalies, it reverses the sign of the velocity contrast, making cold regions slower than piles. As a result, the correlation between Vs and Vb anomalies is small or negative in the lowest ∼300 km, whereas the correlation is positive above this region. Again, anelasticity is not included in seismic anomalies shown in Figure 6; if it were then slow anomalies in Vs would be slightly amplified.

[16] Figure 7 shows temporal variations of thermo-chemical structures for the case with NCFMAS-I. Similar features can be identified at all times, indicating that the thermo-chemical features discussed above for Figure 6 are robust (as in the isochemical cases in Figures 3 and 4).

[17] Figure 8 shows thermo-chemical structures and seismic anomalies for the other three compositional models. The main features in these models, which include large-scale dense piles, plumes rising from the edges of dense piles, and an anti-correlation between Vs and Vb anomalies near the CMB due to the post-perovskite phase, are not very different from those in Figure 5, indicating their robustness to different assumed MORB compositions.

3.3. Local 1-D Radial Seismic Velocity Profiles Without Anelasticity

[18] Figure 9 shows 1-D radial profiles of shear wave and bulk sound velocities from 2000 km depth to the CMB for isochemical convection cases. In order to capture the influence of the laterally varying structure on 1-D seismic profiles, we sample the 2D annulus with 8 profiles separated by 45 degrees in azimuth. We observe two types of discontinuities. First, sharp increases in Vs accompanied by decreases Vb are found between 2650 km to 2700 km. Second, velocity jumps with sharp decreases in Vs and increases Vb are found around 2850 km. These types of velocity jumps are consistent with the mineral physics prediction on the appearance of the post-perovskite phase [*Wookey et al.*, 2005] as well as 1-D seismic structure obtained from waveform analysis beneath the central America [*Hutko et al.*, 2008]. The succession of two discontinuities with opposite polarity is characteristic of the 'double-crossing' caused by the steep Clapeyron slope of the perovskite to post-perovskite phase transition [*Hernlund et al.*, 2005]. This demonstrates the successful inclusion of post-perovskite in the mineral physics databases in this study [*Stixrude and Lithgow-Bertelloni*, 2011]. Note that no seismic discontinuities are found in hot regions (e.g., profile F in simulation NCFMAS-R and profile B in simulation NCFMAS-O) because post-perovskite is not stable at such high temperatures. Using the mineralogical data set provided from *Stixrude and Lithgow-Bertelloni* [2011] and assuming
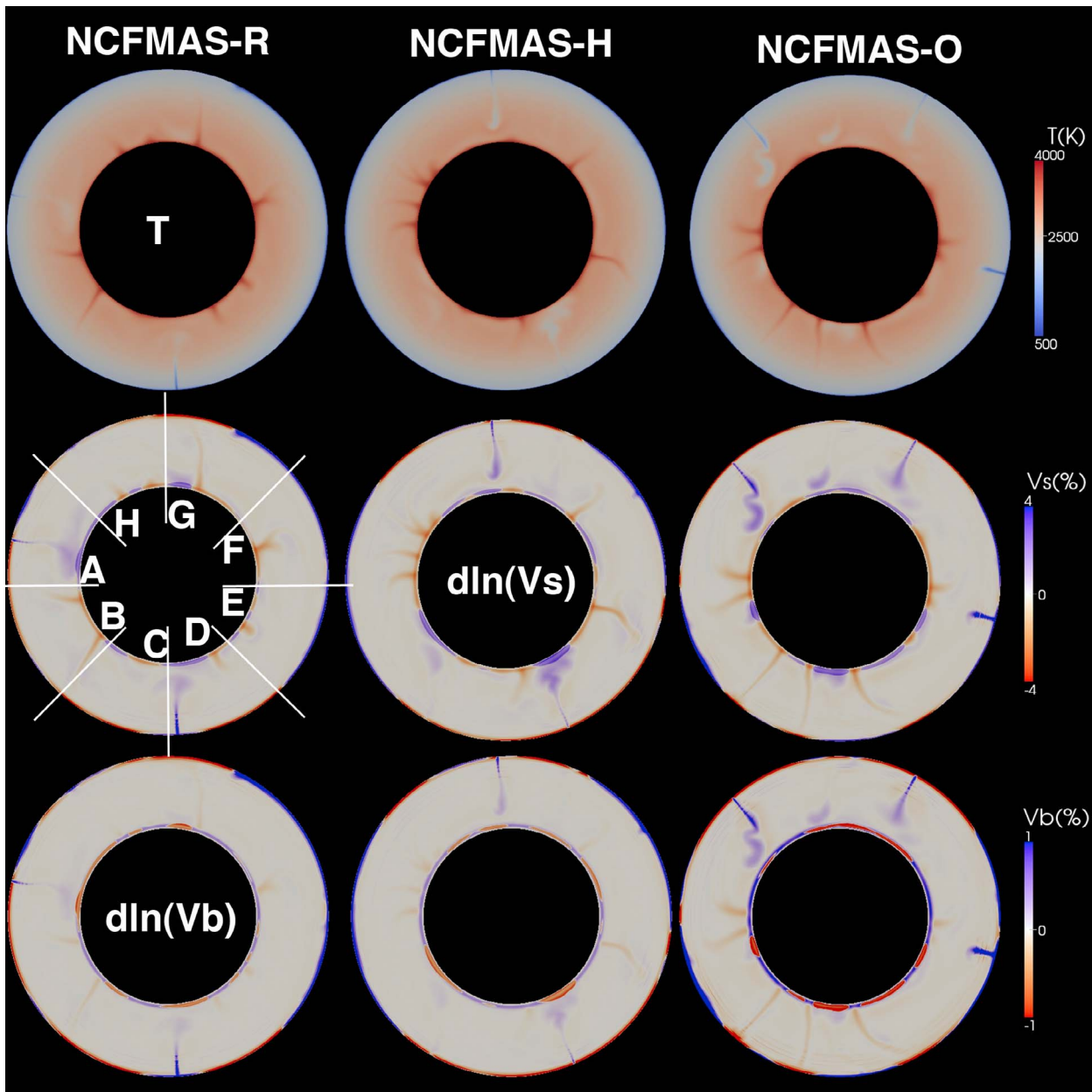
Figure 5. As of Figure 3 for other three compositional models. Section lines shown in NCFMAS-R indicate to use 1-D structures shown in Figure 9.

a mechanical mixture of basalt and harzburgite, post-perovskite is not stable in hot regions near the CMB, leading to either a double-crossing of the phase boundary or no crossing. It is possible that this would be different if an equilibrium assemblage, rather than mechanical mixture, were assumed. If so, this is consistent with the experimental results of *Grocholski et al.* [2012], who find that a sharp Pv- > pPv boundary cannot occur in a pyrolitic equilibrium assemblage, but that it can occur in a differentiated oceanic lithosphere

materials, similar to what we assume here with a mechanical mixture.

[19] Figure 10 shows 1-D seismic profiles for thermo-chemical mantle convection cases. The locations of profiles A to H along the annulus are shown in Figure 4. Again, major velocity jumps at 2600 km to 2850 km are found, which correspond to the post-perovskite phase transition in cold regions. However, for NCFMAS-O, such jumps are not found because the regions of post-perovskite are very
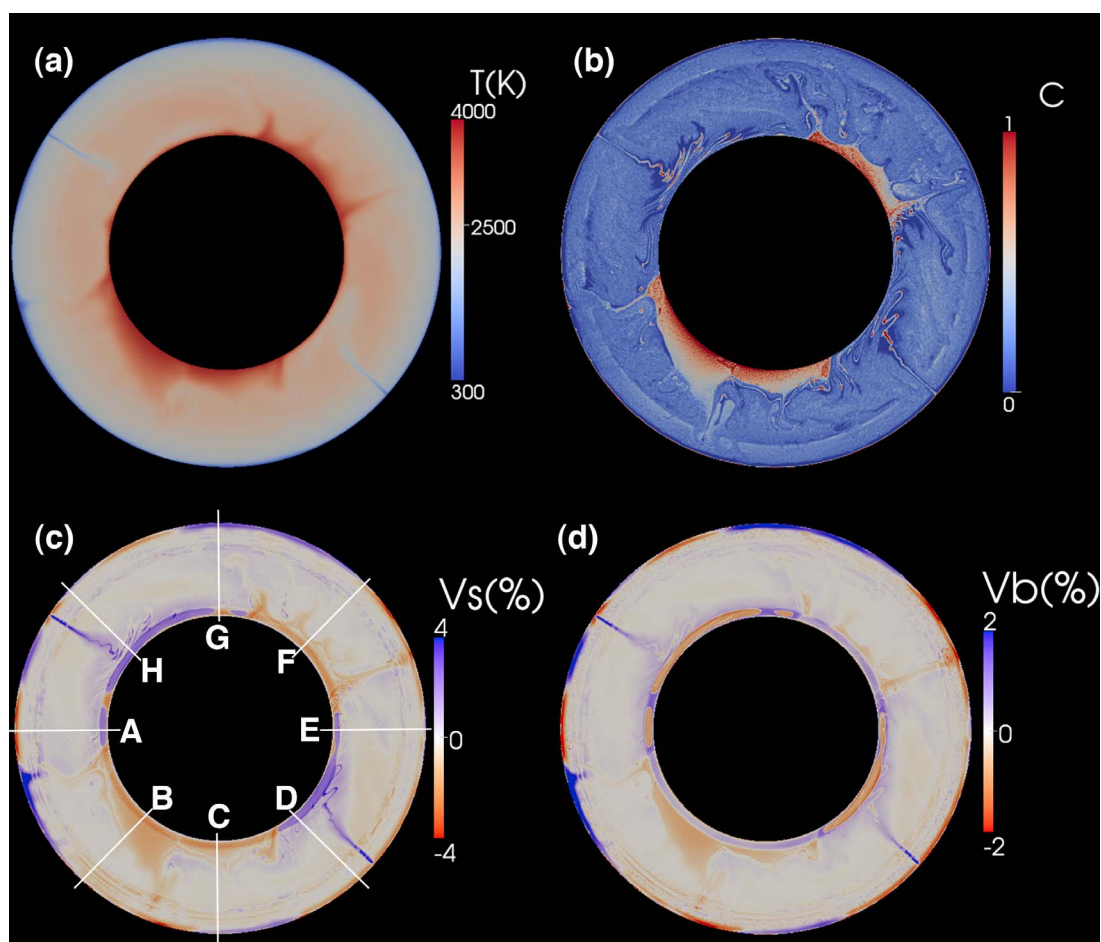
Figure 6. Temperature, composition (red = basalt to dark blue = harzburgite) and shear wave and bulk sound velocity anomalies at t = 4.5 Gyrs for thermo-chemical case of NCFMAS-I. (a) Temperature. (b) Composition. (c) Shear wave anomalies. (d) Bulk sound anomalies. Section lines indicate 1-D structures shown in Figure 10.

localized, and none of them are sampled by our selected profiles (see Figures 3 and 5). In some regions, several minor seismic velocity jumps are indicated at depths shallower than that of the transition to post-perovskite. For example, Figure 11 shows 1-D seismic structure along section H of NCFMAS-R and NCFMAS-I, where the post-perovskite phase is present. The large increase in Vs and decrease in Vb around 2600 km depth indicate the transition from perovskite to post-perovskite. Small kinks in Vs are also found around at 2300, 2400 and 2500 km depth. Kinks in Vb are also observed at the same depths and appear to be of opposite sign to those in versus. These kinks are not caused by the post-perovskite phase transition. Rather, they result from compositional anomalies (i.e., MORB and harzburgite) inside the deformed slab, which is sampled due to the complex slab morphology, as indicated by the slab deformation (Figures 6 and 7). Another example of seismic kinks

is shown in Figure 11b, which plots section H of NCFMAS-I. Again, a large increase in Vs and decrease in Vb are found at 2600 depth, indicating the transition to post-perovskite. From 2350 km to 2450 km, small kinks in Vs are also found, with unclear or weak kinks in Vb. Figure 6 indicates that the cold subducting slab is strongly deformed in this region, thus inducing compositional transitions between MORB and harzburgite, which is the cause of the kinks in the seismic profile. Note that such features are also found in seismic waveform analyses [*Hutko et al.*, 2006].

[20] Figure 12 shows the 1-D seismic structure along section A of NCFMAS-R, and NCFMAS-H, which is located at the edge of a pile of segregated MORB (see Figure 6) at a location where a plume is rising. From 2720 to 2770 km depth, a discontinuity is observed that seems to correspond to the top of the thin basaltic layer; above this Vs is relatively
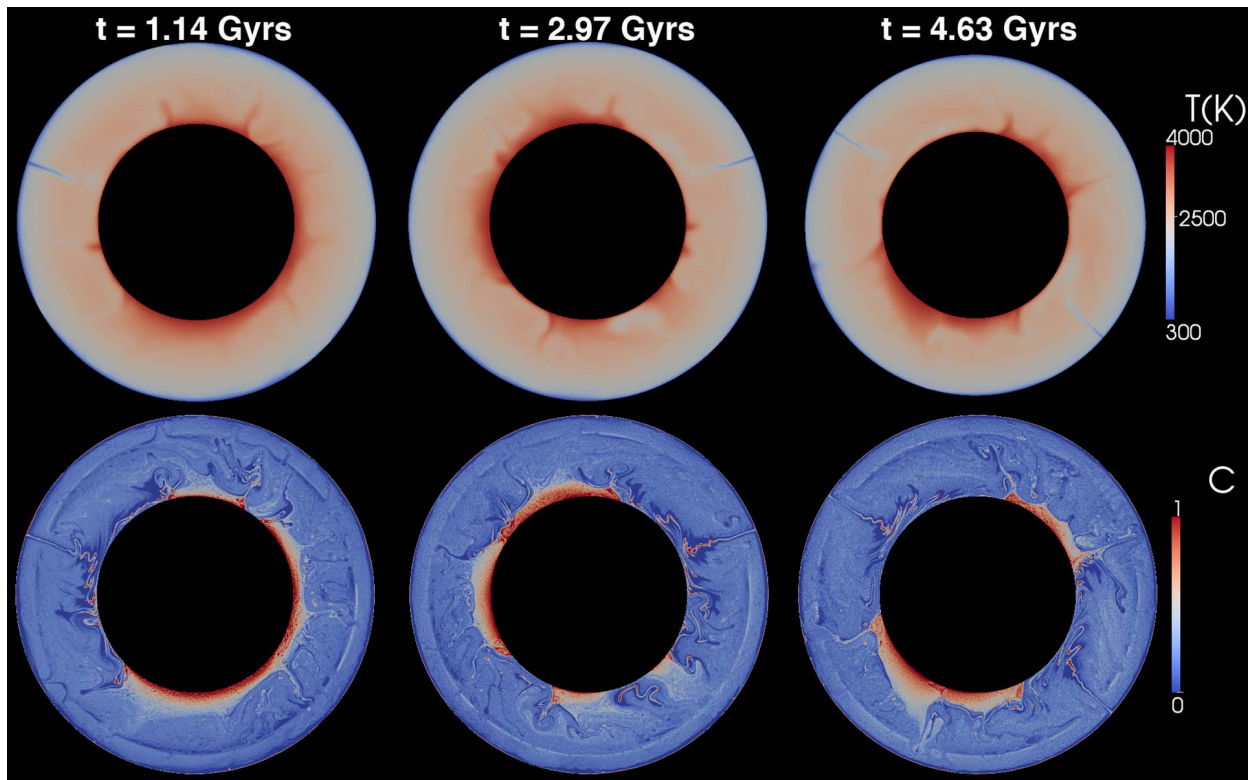
Figure 7. Temporal variation of temperature and composition for a thermo-chemical case of NCFMAS-I.

low because of the plume (Figure 12a). Profile A of NCFMAS-H (Figure 12b) samples a similar region, with a thin MORB layer from which an incipient plume rises. Near 2400 km depth Vs starts decreasing; this corresponds to the top of the incipient plume. A sharp decrease in Vb is present at around 2600 km, which seems to correspond to the top of the thin basaltic layer.

[21] The main conclusion from these profiles is therefore that things other than post-perovskite, namely composition and sharp temperature gradients, can produce discontinuities in the seismic velocity or its radial derivative.

3.4. Effects of Anelasticity

[22] The 1-D seismic profiles discussed in section 3.3 do not account for anelasticity. In order to test how anelasticity affects 1-D seismic structures in the deep mantle, Figure 13 compares 1-D seismic profiles of Vs with and without anelastic effects in two characteristic regions: a cold downwelling (section H of NCFMAS-R) and at the edge of a pile of segregated MORB (section A of NCFMAS-R). In profile A of NCFMAS-R, the velocity including anelasticity decreases significantly below 2600 km. This is a consequence of the strong increase in temperature in

this region, which is caused by the plume; the anelasticity effect is strongly temperature-dependent. In section of H of NCFMAS-R, the velocity profile including anelasticity is not very different from that without anelasticity effects except for below 2800 km depth, where the velocity profile also decreases noticeably compared to the purely elastic case. The maximum difference in Vs is slightly less than 0.1 m/s, which is 1.4%, significant compared to lateral variations caused by temperature. Again, this is linked to the rapid temperature increase in the thermal boundary layer above the CMB. The total decrease of Vs in the lowermost ~50 km is about 0.4 km/s, almost 6%. While this rapid reduction is somewhat reminiscent of an ultra low velocity zone (ULVZ) [*Williams and Garnero*, 1996; *Lay et al.*, 2004], this velocity reduction of 6% is far lower than the 30% inferred for ULVZs [e.g., *Williams and Garnero*, 1996; *Lay et al.*, 2004; *Thorne and Garnero*, 2004; *Idehara et al.*, 2007; *McNamara et al.*, 2010].

[23] The effect of anelasticity on 2D fields of Vs anomaly is shown in Figure 14. Fast regions are not affected, but slow (hot) anomalies are visibly amplified by the anelastic correction, which is as much as 2% for the hottest regions. This does not
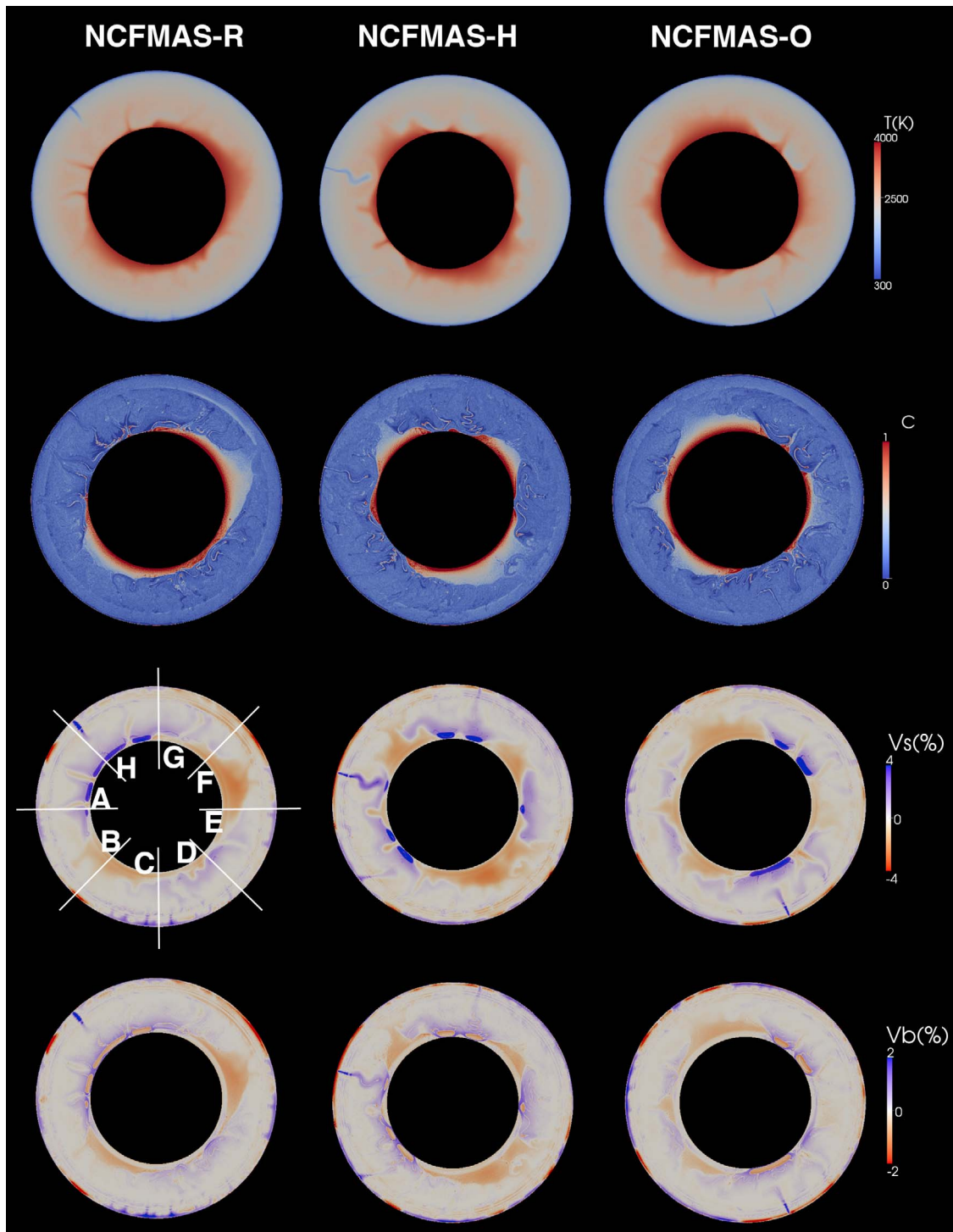
Figure 8. As of Figure 6 for other three compositional models. Section lines for NCFMAS-R are used to show the 1-D seismic structure in Figure 10.

affect conclusions made about the causes of discontinuities observed in 1-D profiles, but may be considered in interpretations of anomalies observed in seismic tomographic models.

[24] As pointed out in previous studies [*Goes et al.*, 2004; *Brodholt et al.*, 2007; *Matas and Bukowinski*, 2007] and reviewed in section 2.1, the sensitivity of anelasticity (or quality factor) to temperature is
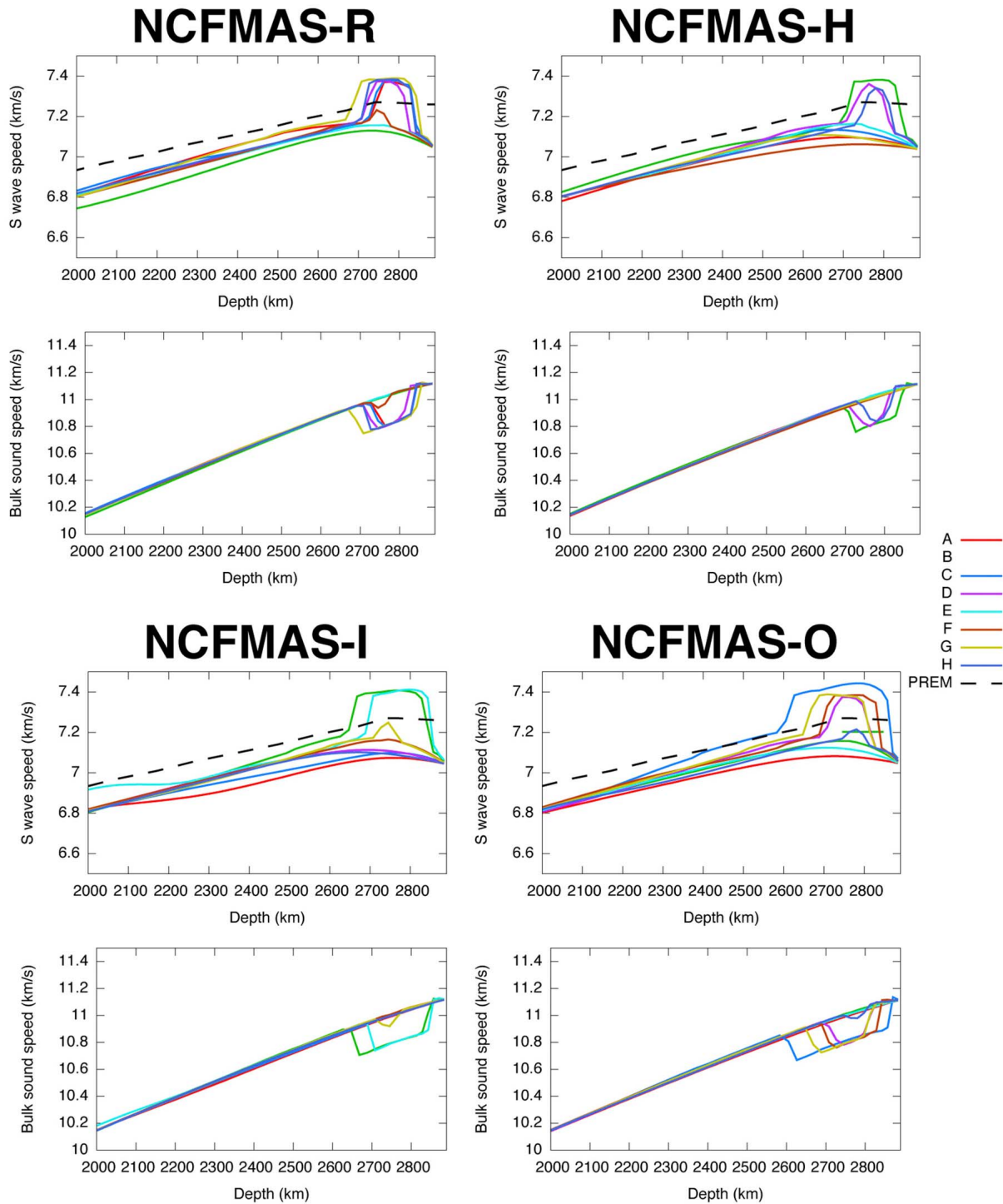
Figure 9. (top row) Local S-wave and (bottom row) bulk sound radial velocity profiles for isochemical cases. Dashed lines are for PREM. Labels A to H corresponds to the lines shown in the Vs anomaly plot for NCFMAS-I of Figure 3.

highly uncertain because of huge uncertainties in the activation energy of the quality factor. Here we test this by trying two additional activation energies (E in equation (2)) while keeping the same V. The

activation energies are intended to represent lower and upper bounds, as identified in [*Goes et al.*, 2004; *Brodholt et al.*, 2007; *Matas and Bukowinski*, 2007]. Our lower bound is 200 kJ/mol, which
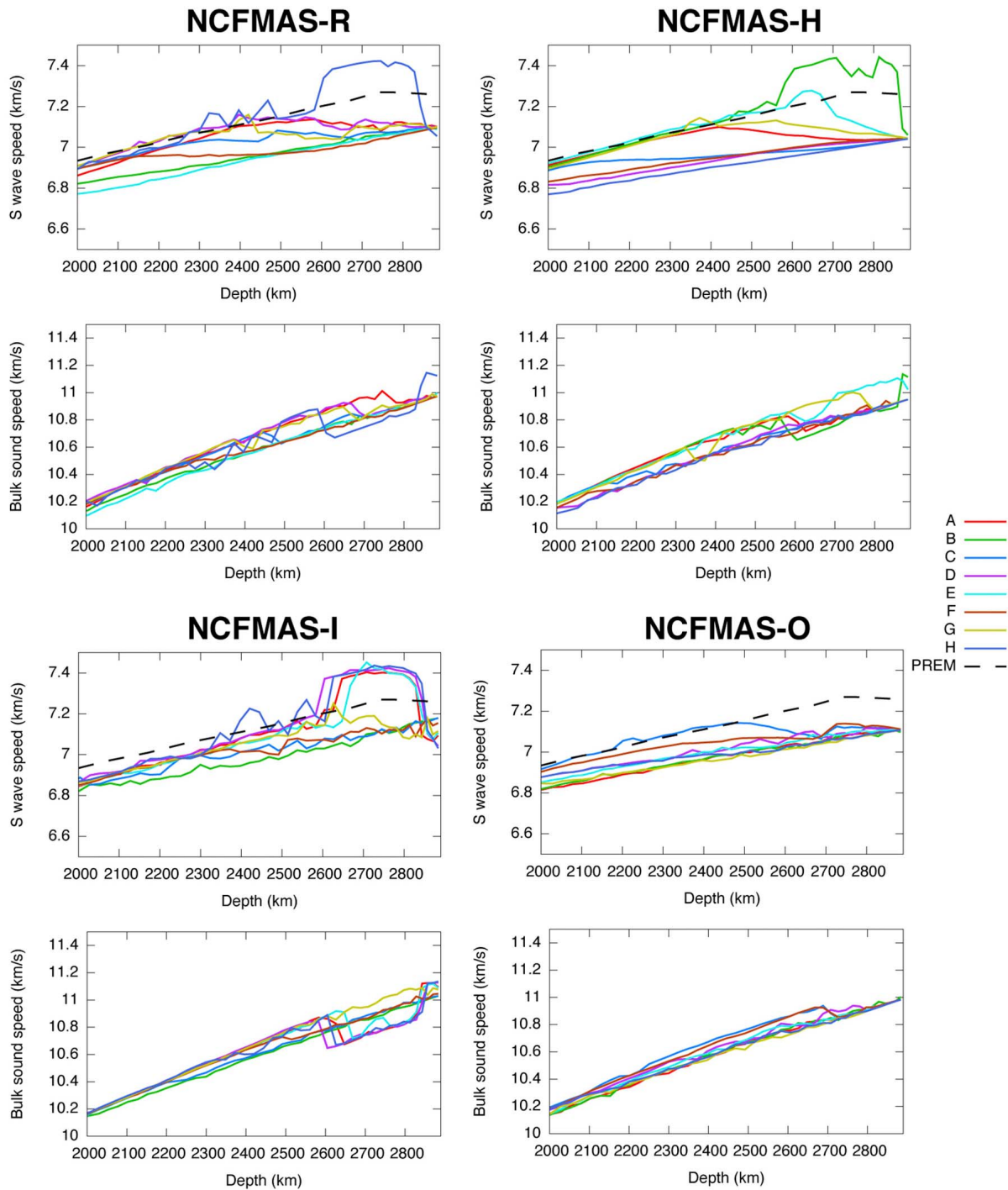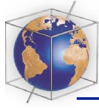
Figure 10. (top row) Local S-wave and (bottom row) bulk sound radial velocity profiles for thermo-chemical cases. Dashed lines are for PREM. Labels A to H corresponds to the lines shown in the S anomaly plot for NCFMAS-I of Figure 6.

gives a lower mantle H* increasing from 237 to 404 kJ/mol; and our upper bound is 500 kJ/mol, which gives a lower mantle H* increasing from 537 to 704 kJ/mol. Figure 15 shows the 1-D seismic structure below 2000 km as a function of

depth for fast and slow anomalous regions. For the lower bound E, the profiles are close to the purely elastic one, whereas for the upper bound the effect is amplified such that the deviation from PREM is approximately doubled. However,
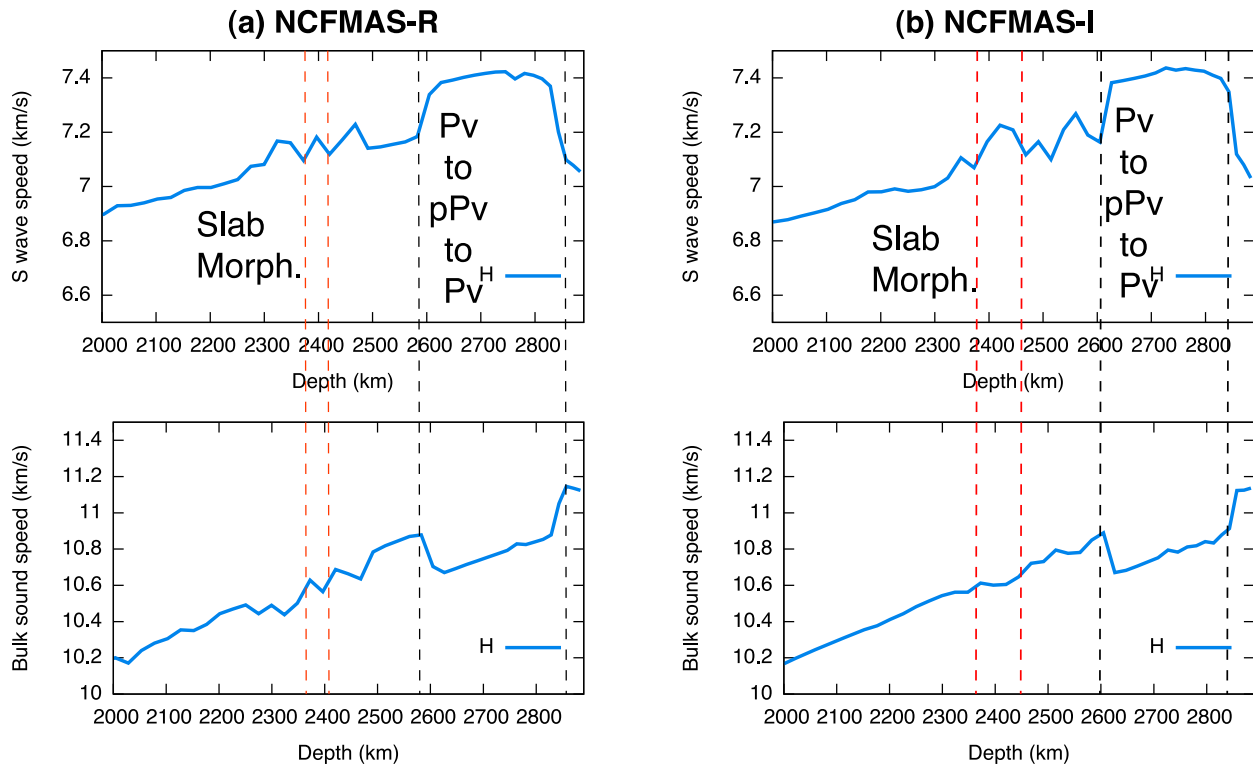
Figure 11. 1-D seismic velocity profiles along line H for NCFMAS-R and NCFMAS-I. Black dashed lines indicate the position of the perovskite to post-perovskite and post-perovskite to perovskite phase transitions. Red dashed lines indicate velocity jumps related to the slab morphology (not related to the post-perovskite transition).

for all values, there is not much effect above the lower thermal boundary layer. These are somewhat consistent with seismic observations [*Hwang and Ritsema*, 2011]. Note that we assume $\alpha = 0.3$ and it could be substantially lower than this (as low as 0.1), which would reduce sensitivities accordingly.

[25] In summary, it should be noted that the effect of anelasticity in the deep mantle is highly uncertain because the parameters describing the quality factor (equation (2)) are not well constrained, as discussed quantitatively in section 2.1 and tested above. Anelastic effects may be small enough that their amplitudes may fit within the error bars due to various sources of uncertainties [e.g., *Trampert et al.*, 2001; *Brodholt et al.*, 2007; *Matas et al.*, 2007].

4. Discussion

4.1. Comparison Between Isochemical and Thermochemical Models

[26] Comparing isochemical and thermochemical models (Figures 3 to 8), the horizontal scale of dynamics in the deep mantle is very different. In particular, isochemical cases are dominated by small-scale structures, partly because the post-perovskite phase transition induces smaller-scale plumes [*Nakagawa and Tackley*, 2004; *Tackley et al.*, 2007]. In contrast, thermo-chemical models are dominated by large-scale structures in the deep mantle. Global tomographic images [e.g., *Masters et al.*, 2000; *Becker and Boschi*, 2002; *Trampert et al.*, 2004; *Houser et al.*, 2008] are dominated by long wavelengths and are therefore, according to the present comparison, better explained by thermo-chemical models than by isochemical models, as was also noted in our previous study [*Nakagawa et al.*, 2010]. A detailed statistical comparison between tomographic models and our synthetic velocity anomalies is, however, beyond the scope of this paper, which focuses on 1-D local seismic profiles. As a quick test we do, however, try reducing the resolution of seismic anomalies to tomographic resolution using a simple filter (see section A2). This shows that large-scale features are preserved at the filtered 'tomographic' resolution while, as expected, narrow features (slabs and plumes) are smeared and their peak anomaly is reduced. This means that our discussion described above may be robust for understanding the
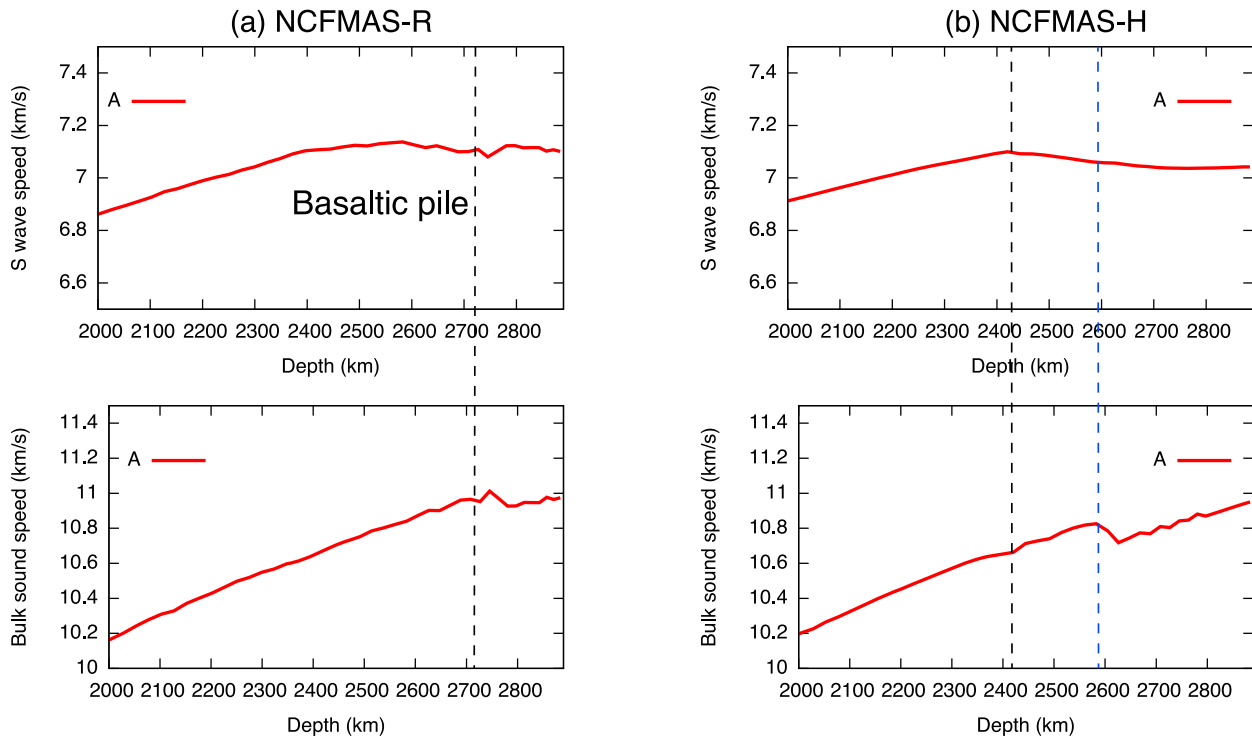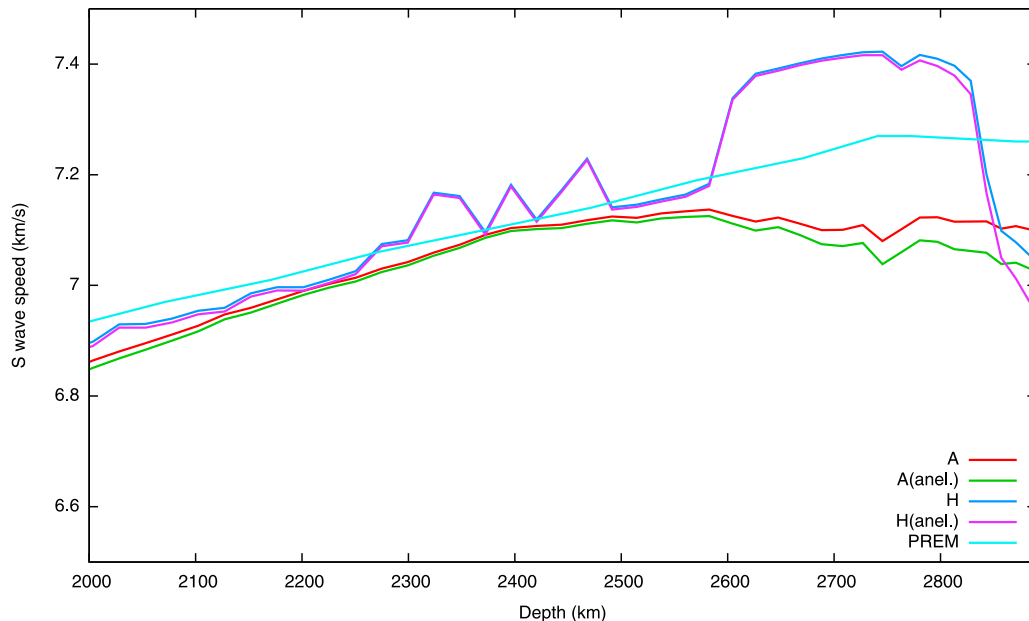
Figure 12. 1-D seismic velocity profiles along line A for NCFMAS-R and NCFMAS-H. Dashed line indicates the boundary between basaltic piles and ambient lower mantle. Black dashed line indicates the position corresponding to the deformed slab caused by basaltic piles. Blue dashed line in Figure 12b indicates the position between basaltic piles and deformed slab.

relationship between seismic anomalies and thermo-chemical structures in the deep mantle.

[27] Some previous studies have constructed seismic velocity anomalies using numerical mantle convection simulations in which plate reconstructions are imposed as a surface boundary condition and 'tomographic filtering' is used to filter the models to tomographic resolution, and have

Figure 13. 1-D seismic velocity profiles with and without anelastic effects for lines A and H for NCFMAS-R.
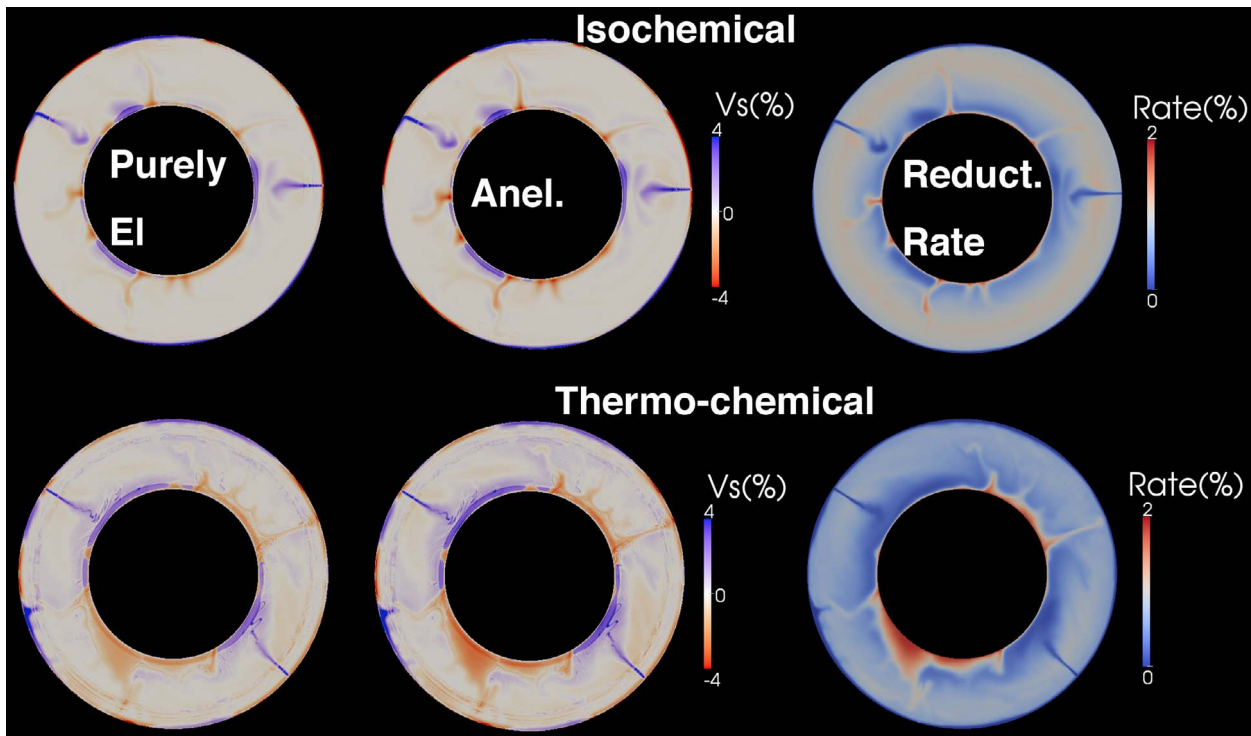
Figure 14. Shear wave anomalies including anelastic effects for NCFMAS-I. (left) Purely elastic properties. (middle) Including anelastic properties. (right) Reduction rate of seismic anomalies.

attributed the anomalies to a purely thermal or sometimes thermo-chemical origin [e.g., *Ritsema et al.*, 2007; *Bull et al.*, 2010; *Schuberth et al.* 2009; *Davies et al.*, 2012].

[28] It should, however, be noted that tomographic models based on normal modes [*Ishii and Tromp*, 1999; *Trampert et al.*, 2004; *Mosca et al.*, 2012], which are a fundamentally different type of observation than body waves, also display LLSVPs with an anti-correlation between Vs and Vb and a density anomaly that suggests chemically dense composition, supporting the interpretation of LLSVPs as thermo-chemical structures.

4.2. Comparison With Seismically Derived Profiles

[29] At the edge of an LLSVP, a reflectivity analysis based on seismic waveform data by *Avants et al.* [2006] suggested the existence of two discontinities related to double-crossing of the perovskite to post-perovskite transition [*Hernlund et al.*, 2005], as well as one additional discontinuity. A subsequent analysis in the same area by *Lay et al.* [2006] obtained profiles with four discontinuities in total: one above and one below the discontinities identified as due to post-perovskite.

Ohta et al. [2008] suggested that all four of these discontinities are due to the perovskite to post-perovskite transition appearing in different compositions (MORB and pyrolite) that are mixed together. However, in our present models, 1-D seismic profiles sampling similar regions near the edge of LLSVPs (Figures 9 and 10) are not influenced by post-perovskite because the temperature is too high. Instead several seismic discontinities related to compositional interfaces (MORB to harzburgite) can be seen, caused by complex deformation of slabs as they interact with the CMB, for example by folding. Other models of 1-D seismic structure for a region at the edge of LLSVPs were obtained by *Konishi et al.* [2009], and were interpreted in terms of the post-perovskite transition occurring inside basaltic piles. Again this is not consistent with our present models, in which post-perovskite is not found inside basaltic piles because the temperature inside the piles is too high, which is partly because of the intrinsic dynamics (see review in *Tackley* [2007]) and partly because heat-producing elements are concentrated into the basaltic material. Another possible explanation for piles of dense material is that they consist of material with a primordial origin [*Deschamps et al.*, 2011, 2012]. The exact mineralogy of such material is still uncertain but, it may be enriched in iron and silicates, as assumed by E-chondrite models of
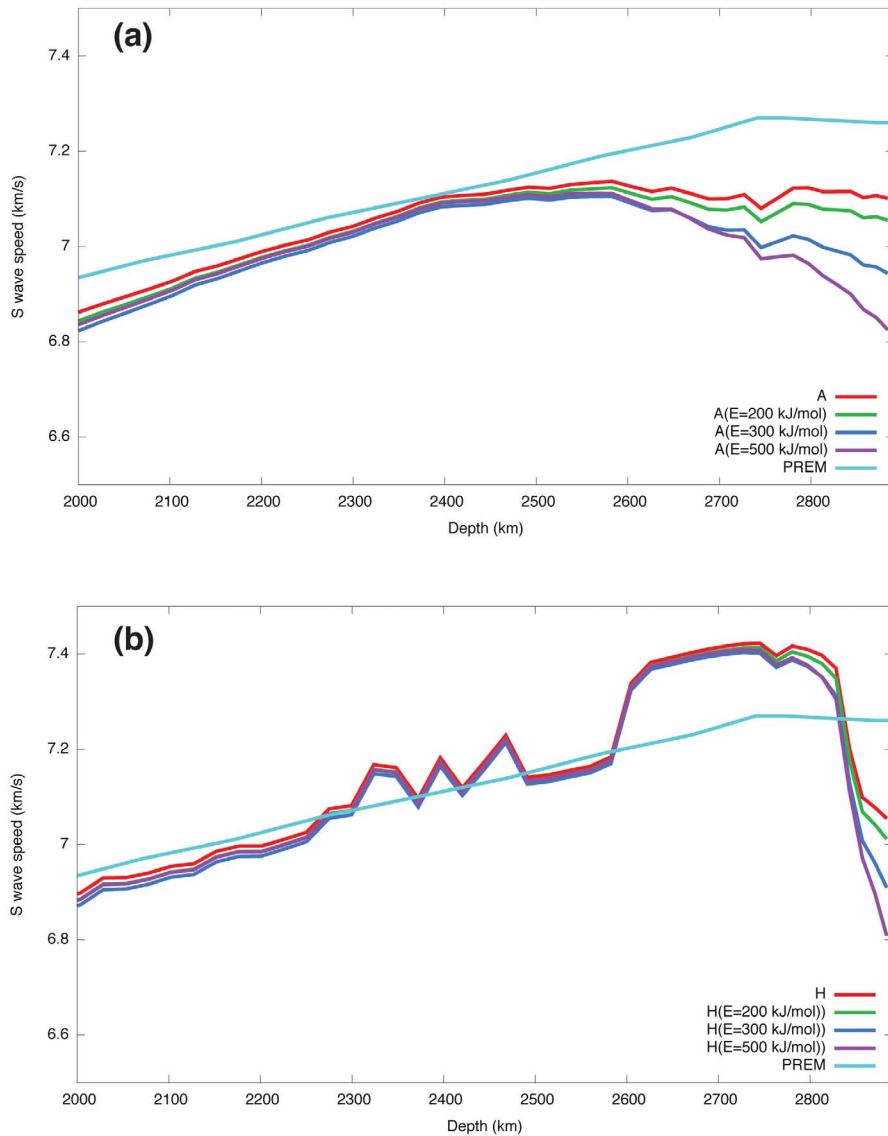
Figure 15. As of Figure 13 including three values of activation energy in equation (2). (top) Line A for NCFMAS-R. (bottom) Line H for NCFMAS-R.

Earth's mantle [*Javoy et al.*, 2010]. Alternatively, pools of primordial material enriched in iron may result in from early partial differentiation of the mantle [e.g., *Labrosse et al.*, 2007; *Tackley*, 2012].

[30] Note that mineral physics results [*Ohta et al.* 2008, *Grocholski et al.*, 2012] indicate that the post-perovskite transition occurs at lower pressure (or higher temperature) in MORB than in pyrolite or harzburgite and therefore it could, in principle, appear in MORB piles even if they are somewhat hotter than surrounding pyrolite or harzburgite. In our present simulations, however, it appears that the MORB piles are hotter by an amount that is too large for this to occur. Furthermore, according to

the database we use, post-perovskite does not have much effect on the seismic properties of MORB, regardless of the exact composition assumed. In future, it would be worth examining in detail to what extent deep mantle properties and phase diagrams calculated using the database of *Stixrude and Lithgow-Bertelloni* [2011], are consistent with the range of mineral physics results including the latest [*Grocholski et al.*, 2012]. Another possibility to evaluate is that if we were to include greater temperature-dependence of viscosity then the piles would be less hot, allowing post-perovskite to appear. However, it is not clear whether greater temperature-dependence of viscosity would make the piles hotter or cooler: on the one hand it would

lead to more efficient heat transfer to the mantle above, potentially decreasing the temperature contrast with the mantle above (as in, e.g., the parameterized models of *McNamara and van Keken* [2000]); on the other hand it would also increase heat transfer from the core, potentially decreasing the temperature contrast with the core (as in, e.g., *Solomatov and Moresi* [2002]).

[31] In cold regions near the CMB, *Hutko et al.* [2008] seismically observed an anti-correlation between shear wave and bulk sound (or compressional wave) velocity, consistent with the mineral physics prediction [*Wookey et al.*, 2005]. Such an anti-correlation is also observed in 1-D seismic profiles from our numerical mantle convection simulations (see Figures 7 and 8). In the same cold region, *Kawai et al.* [2007] performed waveform inversion to obtain 1-D S-wave velocity profiles and found evidence for a double-crossing of the post-perovskite transition; similar evidence was later found in a cold region under Asia [*Kawai et al.*, 2009]. The amplitude of the velocity jump found in our experiments is 3% for shear velocity and 1.8% for bulk sound velocity, which are consistent with results from ab initio calculations [*Wookey et al.*, 2005] but a factor of two larger than found by seismic waveform analysis [*Hutko et al.*, 2008].

[32] In our present experiments, seismic discontinuities are related to compositional discontinuities in a folded slab, which, in a broad sense, they are consistent with the seismic waveform analyses of *Hutko et al.* [2006], who found a stepped discontinuity that they attributed to a folded slab. This means that seismic discontinuities are not always related to the solid-solid phase transition of perovskite to post-perovskite.

4.3. Influence of Anelasticity on 1-D Seismic Structures

[33] The main anelastic effect we obtain is a significant reduction of the shear wave velocity near the CMB because of the strong temperature dependence of anelasticity combined with the strong increase of temperature in the lower thermal boundary layer. However, we find that anelastic effects are not significant for 1-D profiles above this boundary layer, which means above 2800 km depth for cold regions and above 2600 km depth for hot regions. This means that anelastic effects do not affect the position and amplitude of the velocity jump caused by the post-perovskite phase transition and the boundary between basaltic piles and ambient lower mantle. Therefore, including anelastic effects into 1-D

seismic structures in the deep mantle does not change the main conclusions discussed in previous sections.

[34] A recent attempt at determining the attenuation structure in the deep mantle indicated that the attenuation in the deepest part of the mantle (below about 2500 km depth) could not be constrained seismologically due to the interference of P and S and the core-reflections PcP and ScS at the corresponding large distances [*Hwang and Ritsema*, 2011]. This means that predictions of the velocity reduction below 2600 km due to anelasticity have huge uncertainties, and any comparison with seismically obtained profiles should be treated with caution.

5. Conclusions

[35] In this study, we have calculated 1-D seismic structure in the deep mantle in numerical thermal or thermo-chemical mantle convection simulations with a self-consistently calculated mineralogy including the post-perovskite phase. The conclusions are as follows:

[36] 1. Isochemical mantle convection including the post-perovskite phase is characterized by small-scale plumes rising from the core-mantle boundary region. This is consistent with early studies on mantle dynamics including the post-perovskite phase transition [*Nakagawa and Tackley*, 2004; *Tackley et al.*, 2007]. This makes it difficult for isochemical mantle convection to explain the characteristic large horizontal scale observed in global seismic tomographic models, even when filtered to seismic resolution as shown in Appendix A. This suggests that thermo-chemical models are better for explaining the horizontal length-scale of global tomographic images, but more investigation is needed using a joint seismological-mineral physics-geodynamical approach.

[37] 2. The post-perovskite phase further increases the shear wave velocity anomaly in 'fast' regions containing pooled slabs while making these regions slow in bulk sound velocity, thereby generating an anti-correlation between Vs and Vb in the lowest ~300 km. This is consistent with mineral physics predictions [*Wookey et al.*, 2005] and 1-D seismic structures beneath the central America [*Hutko et al.*, 2008]. However, the post-perovskite phase is not noticed in basaltic piles because the temperature in these piles is too high, even though the post-perovskite transition occurs at higher temperature in MORB compared to harzburgite.
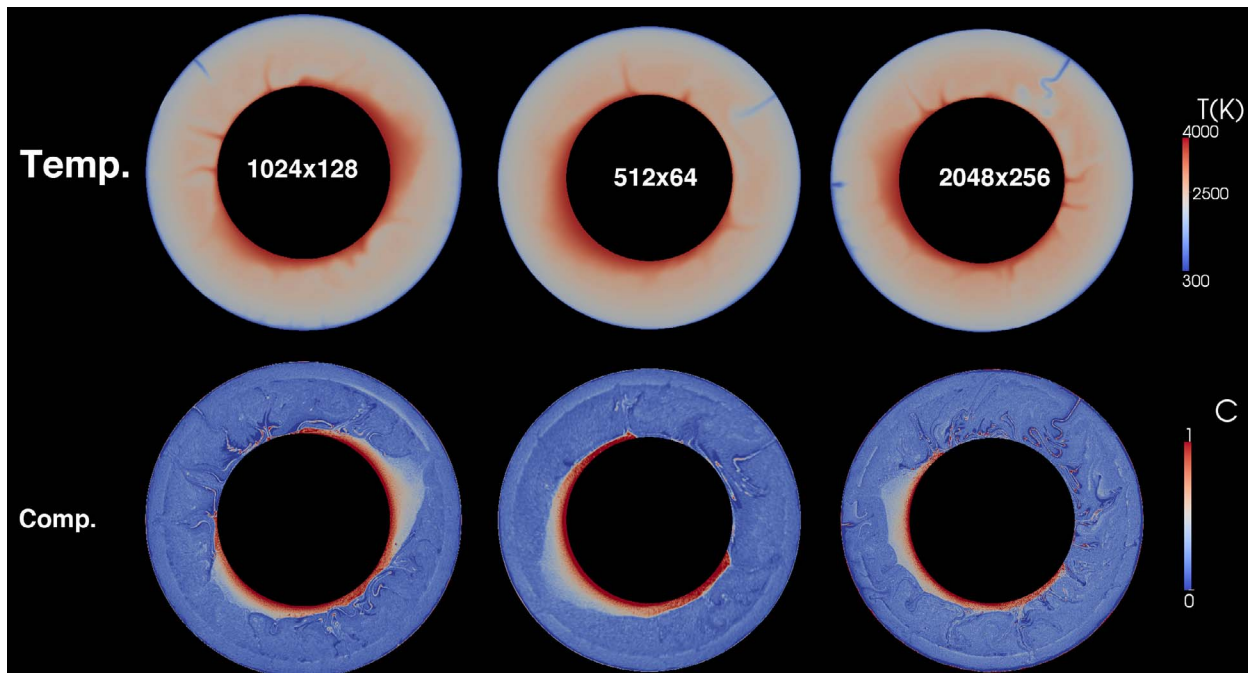
Figure A1. Numerical resolution dependence of thermo-chemical structures for NCFMAS-R.

[38] 3. Examining local 1-D radial profiles of Vs or Vb, while a double discontinuity due to post-perovskite is observed in cold areas, discontinuities are also observed that are unrelated to post-perovskite, and are instead caused by compositional discontinuities (MORB to harzburgite), particularly in regions where folded slabs occur above the CMB. This can be also found in regional three-dimensional models [*Tackley*, 2011]. Thus, careful interpretation is needed of seismic studies that find up to three or four seismic discontinuities in the CMB region [e.g., *Avants et al.*, 2006; *Lay et al.*, 2006; *Ohta et al.*, 2008]. In order to understand deep mantle dynamics, it is necessary to combine seismology, mineral physics and mantle dynamics.

[39] 4. Anelasticity does not affect interpretations of 1-D seismic structures in the deep mantle calculated from the mantle convection simulations in this study because the influence on seismic velocities is quite small except at the high temperatures close to the CMB.

[40] In this study, we focus on 1-D seismic profiles in the deep mantle obtained in numerical mantle convection simulations. These results demonstrate the importance of using a joint geodynamical-mineralogical approach to predict and aid in the interpretation of deep mantle seismic structure, because interpretations based on seismology and mineral physics alone may be misleading due to not predicting the strong lateral variability and locality of

1-D structure obtained here: for example, multiple reflections arising from folded slabs and the precise balance between thermal and compositional influences on seismic structure such as in large low velocity seismic provinces. Such models are also useful for computing various statistical diagnostics to compare with those from global seismic tomographic models, as was investigated for example by *Della Mora et al.* [2011]. We will study and compare such diagnostics in the next paper.

Appendix A: Resolution and Filtering Tests

A1. Resolution Test for Numerical Resolution

[41] In order to check the robustness of the obtained structures to numerical resolution, we test two different resolutions that are lower and higher than our default: 512×64 and 2048×256 cells, respectively. Figure A1 shows thermo-chemical structures at 4.6 Gyrs for NCFMAS-R with three resolutions. The general character of the solutions is not much influenced by resolution, with piles of segregated MORB, folded slabs, etc. For our target in this study, which is 1-D radial profiles, the resolution does not make much difference to the character and type of structures obtained. Good radial resolution is needed to obtain sharp discontinuities in 1-D radial profiles.
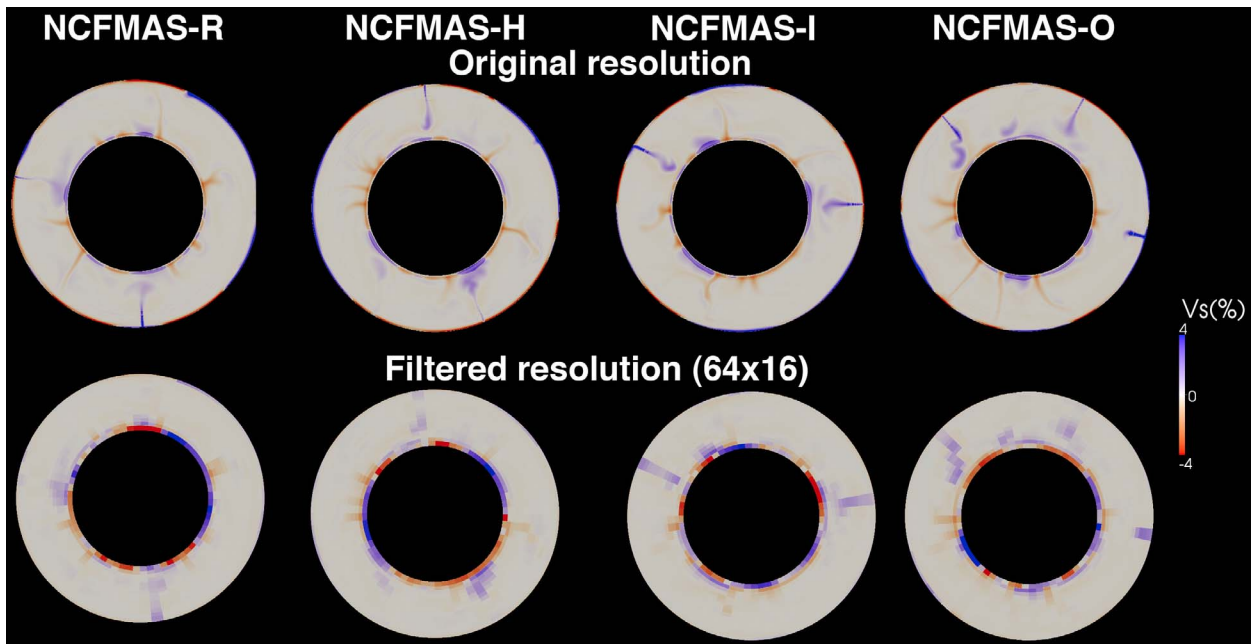
Figure A2. (top) Vs anomalies for isochemical cases with actual numerical resolution. (bottom) Those for filtered resolution.

A2. Filtering to Seismic Resolution

[42] Our target seismological comparison in this study is 1-D radial profiles obtained from waveform modeling, for which quite good radial resolution can be obtained. However, it is also interesting to compare to seismic tomography, which has a much coarser effective resolution. Some studies, in which plate reconstructions are imposed at the top boundary, have degraded the resolution by applying a 'tomographic filter' using the resolution matrix from an actual seismic tomographic inversion [*Ritsema et al.*, 2007; *Schuberth et al.*, 2009; *Bull et al.*, 2010; *Davies et al.*, 2012]. Here, because our models are not intended to reproduce the exact configuration of the present-day Earth, we use a simpler
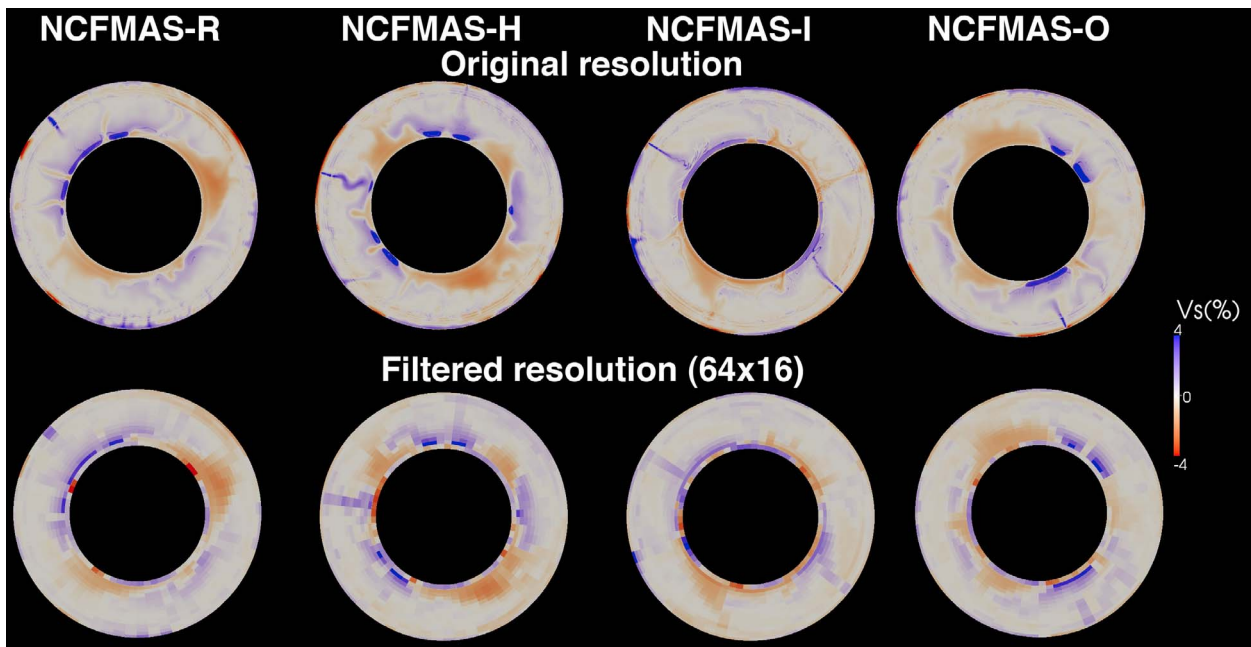
Figure A3. As of Figure A2 for thermo-chemical cases.

filtering method, simply averaging the seismic anomalies to 1/16 of the actual numerical resolution in the horizontal and 1/8 in the radial direction, i.e., 64×16; corresponding to 32 spherical harmonics with 16 layered in the radial direction, which is consistent with that form one of the latest global tomography model [*Ritsema et al.*, 2011], as shown in Figure A2 for isochemical cases and Figure A3 for thermo-chemical cases. Figures A2 and A3 indicate that the main large-scale deep mantle features are well reproduced even at the filtered resolution, but narrow features (slabs and plumes) are substantially blurred and reduced in peak amplitude. Of course, 1-D local radial profiles would be substantially blurred, but seismologically these are not obtained by tomography so this is not a relevant concern.

Acknowledgments

References

Avants, M., T. Lay, S. A. Russell, and E. J. Garnero (2006), Shear velocity variation within the D″ region beneath the central Pacific, *J. Geophys. Res.*, *111*, B05305, doi:10.1029/2004JB003270.

Becker, T. W., and L. Boschi (2002), A comparison of tomographic and geodynamics mantle models, *Geochem. Geophys. Geosyst.*, *3*(1), 1003, doi:10.1029/2001GC000168.

Brandenburg, J. P., E. H. Hauri, P. E. van Keken, and C. J. Ballentine (2008), A multiple-system study for the geochemical evolution of the mantle with force-balanced plates and thermochemical effects, *Earth Planet. Sci. Lett.*, *276*, 1–13, doi:10.1016/j.epsl.2008.08.027.

Brodholt, J. P., G. Helffrich, and J. Trampert (2007), Chemical versus thermal heterogeneity in the lower mantle: The most likely role of anelasticity, *Earth Planet. Sci. Lett.*, *262*, 429–437, doi:10.1016/j.epsl.2007.07.054.

Bull, A. L., A. K. McNamara, T. W. Becker, and J. Ritsema (2010), Global scale models of the mantle flow field predicted by synthetic tomography models, *Phys. Earth Planet. Inter.*, *182*, 129–138, doi:10.1016/j.pepi.2010.03.004.

Connolly, J. A. D. (2005), Computation of phase equilibria by linear programming: A tool for geodynamic modeling and its application to subduction zone decarbonation, *Earth Planet. Sci. Lett.*, *236*, 524–541, doi:10.1016/j.epsl.2005.04.033.

Connolly, J. A. D. (2009), The geodynamics equation of state: What and how, *Geochem. Geophys. Geosyst.*, *10*, Q10014, doi:10.1029/2009GC002540.

Davies, D. R., S. Goes, J. H. Davies, B. S. A. Schuberth, H.-P. Bunge, and J. Ritsema (2012), Reconciling dynamic and seismic models of Earth's lower mantle: The dominant role of thermal heterogeneity, *Earth Planet. Sci. Lett.*, *353–354*, 253–269, doi:10.1016/j.epsl.2012.08.016.

Della Mora, S., L. Boschi, P. J. Tackley, T. Nakagawa, and D. Giardini (2011), Low seismic resolution cannot explain S/P decorrelation, *Geophys. Res. Lett.*, *38*, L12303, doi:10.1029/2011GL047559.

Deschamps, F., E. Kaminski, and P. J. Tackley (2011), The deep origin for the primitive signature of ocean island basalt, *Nat. Geosci.*, *4*, 879–882, doi:10.1038/ngeo1295.

Deschamps, F., L. Cobden, and P. J. Tackley (2012), The primitive nature of large low shear-wave velocity provinces, *Earth Planet. Sci. Lett.*, *349–350*, 198–208, doi:10.1016/j.epsl.2012.07.012.

Dziewonski, A. M., and D. L. Anderson (1981), Preliminary reference Earth model, *Phys. Earth Planet. Inter.*, *25*, 297–356, doi:10.1016/0031-9201(81)90046-7.

Garnero, E. J., and A. K. McNamara (2008), Structure and dynamics of Earth's lower mantle, *Science*, *320*, 626–628.

Goes, S., R. Govers, and P. Vacher (2000), Shallow mantle temperatures under Europe from P and S wave tomography, *J. Geophys. Res.*, *105*, 11,153–11,169, doi:10.1029/1999JB900300.

Goes, S., F. Cammarano, and U. Hansen (2004), Synthetic seismic signature of thermal mantle plumes, *Earth Planet. Sci. Lett.*, *218*, 403–419, doi:10.1016/S0012-821X(03)00680-0.

Grocholski, B., K. Catalli, S.-H. Shim, and V. Prakapenka (2012), Mineralogical effects on the detectability of the post-perovskite boundary, *Proc. Natl. Acad. Sci. U. S. A.*, *109*(7), 2275–2279, doi:10.1073/pnas.110920410.

Hernlund, J. W., and P. J. Tackley (2008), Modeling mantle convection in the spherical annulus, *Phys. Earth Planet. Int.*, *171*, 48–54, doi:10.1016/j.pepi.2008.07.037.

Hernlund, J., C. Thomas, and P. J. Tackley (2005), Phase boundary double-crossing and partial melting in Earth's deepest mantle, *Nature*, *434*, 882–886, doi:10.1038/nature03472.

Hirose, K., N. Takafuji, N. Sata, and Y. Ohishi (2005), Phase transition and density of subducted MORB crust in the lower mantle, *Earth Planet. Sci. Lett.*, *237*, 239–251, doi:10.1016/j.epsl.2005.06.035.

Houser, C., G. Masters, P. Shearer, and G. Laske (2008), Shear and compressional velocity models of mantle from cluster analysis, *Geophys. J. Int.*, *174*, 178–194, doi:10.1111/j.1365-246X.2008.03719.x.

Hutko, A., T. Lay, E. Garnero, and J. S. Revenaugh (2006), Seismic detection of folded, subducted lithosphere at the core-mantle boundary, *Nature*, *441*, 333–336, doi:10.1038/nature04757.

Hutko, A. R., T. Lay, J. Revenaugh, and E. J. Garnero (2008), Anticorrelated seismic velocity anomalies from post-perovskite in the lowermost mantle, *Science*, *320*, 1070–1074, doi:10.1126/science.1155822.

Hwang, Y. K., and J. Ritsema (2011), Radial Q_μ structure of the lower mantle from teleseismic body-wave spectra, *Earth Planet. Sci. Lett.*, *303*, 369–375, doi:10.1016/j.epsl.2011.01.023.

Idehara, K., A. Yamada, and D. Zhao (2007), Seismological constraints on ultralow-velocity zones in the lowermost mantle from core-reflected waves, *Phys. Earth Planet. Inter.*, *165*, 25–46, doi:10.1016/j.pepi.2007.07.005.

Irifune, T., and A. E. Ringwood (1993), Phase transformations in subducted oceanic crust and buoyancy relationship at depths of 600–800 km in the mantle, *Earth Planet. Sci. Lett.*, *117*, 101–110, doi:10.1016/0012-821X(93) 90120-X.

Ishii, M., and J. Tromp (1999), Normal-mode and free-air gravity constraints on lateral variations in velocity and density of Earth's mantle, *Science*, *285*, 1231–1236, doi:10.1126/science.285.5431.1231.

Javoy, M., et al. (2010), The chemical composition of the Earth: Enstatite chondrite model, *Earth Planet. Sci. Lett.*, *293*, 259–268, doi:10.1016/j.epsl.2010.02.033.

Kawai, K., N. Takeuchi, R. J. Geller, and N. Fuji (2007), Possible evidence for a double crossing phase transition in D″ beneath central America from inversion of seismic waveforms, *Geophys. Res. Lett.*, *34*, L09314, doi:10.1029/2007GL029642.

Kawai, K., S. Sekine, N. Fuji, and R. J. Geller (2009), Waveform inversion for D″ structure beneath northern Asia using Hi-net tiltmeter data, *Geophys. Res. Lett.*, *36*, L20314, doi:10.1029/2009GL039651.

Khan, A., L. Boschi, and J. A. D. Connolly (2011), Mapping the Earth's thermochemical and anisotropic structure using global surface wave data, *J. Geophys. Res.*, *116*, B01301, doi:10.1029/2010JB007828.

Konishi, K., K. Kawai, R. J. Geller, and N. Fuji (2009), MORB in the lowermost mantle beneath the western Pacific: Evidence from waveform inversion, *Earth Planet. Sci. Lett.*, *278*, 219–225, doi:10.1016/j.epsl.2008.12.002.

Labrosse, S., J. W. Hernlund, and N. Coltice (2007), A crystallizing dense magma ocean at the base of the Earth's mantle, *Nature*, *450*, 866–869, doi:10.1038/nature06355.

Lay, T., E. J. Garnero, and Q. Williams (2004), Partial melting in a thermo-chemical boundary layer at the base of the mantle, *Phys. Earth Planet. Inter.*, *146*, 441–467, doi:10.1016/j.pepi.2004.04.004.

Lay, T., J. Hernlund, E. J. Garnero, and M. S. Thorne (2006), A post-perovskite lens and D″ heat flux beneath the central Pacific, *Science*, *314*, 1272–1276, doi:10.1126/science.1133280.

Masters, G., G. Laske, H. Bolton, and A. M. Dziewonski (2000), The relative behavior of shear velocity, bulk sound speed, and compressional velocity in the mantle: Implications for chemical and thermal structure, in *Earth's Deep Interior: Mineral Physics and Tomography From the Atomic to the Global Scale, Geophys. Monogr. Ser.*, vol. 117, edited by S. Karato et al., pp. 63–87, AGU, Washington, D. C., doi:10.1029/GM117p0063.

Matas, J., and M. Bukowinski (2007), On the anelastic contribution to the temperature dependence of lower mantle seismic velocities, *Earth Planet. Sci. Lett.*, *259*, 51–65, doi:10.1016/j.epsl.2007.04.028.

Matas, J., J. D. Bass, Y. Ricard, E. Mattern, and M. S. T. Bukowinski (2007), On the bulk composition of the lower mantle: Predictions and limitations from generalized inversion of radial seismic profiles, *Geophys. J. Int.*, *170*, 764–780, doi:10.1111/j.1365-246X.2007.03454.x.

McNamara, A. K., and P. E. van Keken (2000), Cooling of the Earth: A parameterized convection study of whole versus layered models, *Geochem. Geophys. Geosyst.*, *1*(11), 1027, doi:10.1029/2000GC000045.

McNamara, A. K., E. J. Garnero, and S. Rost (2010), Tracking deep mantle reservoirs with ultra-low velocity zones, *Earth Planet. Sci. Lett.*, *299*, 1–9, doi:10.1016/j.epsl.2010.07.042.

Mosca, I., L. Cobden, A. Deuss, J. Ritsema, and J. Trampert (2012), Seismic and mineralogical structures of the lower mantle from probabilistic tomography, *J. Geophys. Res.*, *117*, B06304, doi:10.1029/2011JB008851.

Nakagawa, T., and P. J. Tackley (2004), Effects of a perovskite-post perovskite phase change near the core-mantle boundary in compressible mantle convection, *Geophys. Res. Lett.*, *31*, L16611, doi:10.1029/2004GL020648.

Nakagawa, T., and P. J. Tackley (2005), The interaction between the post-perovskite phase change and a thermo-chemical boundary layer near the core-mantle boundary, *Earth Planet. Sci. Lett.*, *238*, 204–216, doi:10.1016/j.epsl.2005.06.048.

Nakagawa, T., and P. J. Tackley (2006), Three-dimensional structures and dynamics in the deep mantle: Effects of post-perovskite phase change and deep mantle layering, *Geophys. Res. Lett.*, *33*, L12S11, doi:10.1029/2006GL025719.

Nakagawa, T., P. J. Tackley, F. Deschamps, and J. A. D. Connolly (2009), Incorporating self-consistently calculated mineral physics into thermochemical mantle convection simulations in a 3-D spherical shell and its influence on seismic anomalies in Earth's mantle, *Geochem. Geophys. Geosyst.*, *10*, Q03004, doi:10.1029/2008GC002280.

Nakagawa, T., P. J. Tackley, F. Deschamps, and J. A. D. Connolly (2010), The influence of MORB and harzburgite composition on thermo-chemical mantle convection in a 3D spherical shell with self-consistently calculated mineral physics, *Earth Planet. Sci. Lett.*, *296*, 403–412, doi:10.1016/j.epsl.2010.05.026.

Ohta, K., K. Hirose, T. Lay, N. Sata, and Y. Ohishi (2008), Phase transition in pyrolite and MORB at lowermost mantle convections: Implications for a MORB-rich pile above the core-mantle boundary, *Earth Planet. Sci. Lett.*, *267*, 107–117, doi:10.1016/j.epsl.2007.11.037.

Ono, S., Y. Ohishi, M. Isshiki, and T. Watanuki (2005), In situ X-ray observations of phase assemblages in peridotite and basalt compositions: Implications for density of subducted oceanic plate, *J. Geophys. Res.*, *110*, B02208, doi:10.1029/2004JB003196.

Ricolleau, A., J.-P. Perrillat, G. Fiquet, I. Daniel, J. Matas, A. Addad, N. Menguy, H. Cardon, M. Mezouar, and N. Guignot (2010), Phase relations and equation of state of a natural MORB: Implications for the density profile of subducted oceanic crust in the Earth's lower mantle, *J. Geophys. Res.*, *115*, B08202, doi:10.1029/2009JB006709.

Ringwood, A. E. (1985), Mantle dynamics and basalt petrogenesis, *Tectonophysics*, *112*, 17–34, doi:10.1016/0040-1951(85)90170-2.

Ritsema, J., A. K. McNamara, and A. L. Bull (2007), Tomographic filtering of geodynamic models: Implications for model interpretation and large-scale mantle structure, *J. Geophys. Res.*, *112*, B01303, doi:10.1029/2006JB004566.

Ritsema, J., A. Deuss, H. J. van Heijst, and J. H. Woodhouse (2011), S40RTS: A degree-40 shear-velocity model for the mantle from new Rayleigh wave dispersion, teleseismic traveltime and normal-mode splitting function measurements, *Geophys. J. Int.*, *184*, 1223–1236, doi:10.1111/j.1365-246X.2010.04884.x.

Schuberth, B. S. A., H.-P. Bunge, and J. Ritsema (2009), Tomographic filtering of high-resolution mantle circulation models: Can seismic heterogeneity be explained by temperature alone?, *Geochem. Geophys. Geosyst.*, *10*, Q05W03, doi:10.1029/2009GC002401.

Shim, S.-H., K. Catalli, J. Hustoft, A. Kubo, V. B. Prakapenka, W. A. Caldwell, and M. Kunz (2008), Crystal structure and thermoelastic properties of $(Mg_{0.91}Fe_{0.09})SiO_3$ postperovskite up to 135 GPa and 2,700 K, *Proc. Natl. Acad. Sci. U. S. A.*, *105*, 7382–7386.

Simmons, N. A., A. M. Forte, L. Boschi, and S. P. Grand (2010), GyPSuM: A joint tomographic model of mantle density and seismic wave speeds, *J. Geophys. Res.*, *115*, B12310, doi:10.1029/2010JB007631.

Solomatov, V. S., and L.-N. Moresi (2002), Small-scale convection in the D″ layer, *J. Geophys. Res.*, *107*(B1), 2016, doi:10.1029/2000JB000063.

Stixrude, L., and C. Lithgow-Bertelloni (2005), Thermodynamics of mantle minerals-1. Physical properties, *Geophys. J. Int.*, *162*, 610–632, doi:10.1111/j.1365-246X.2005.02642.x.

Stixrude, L., and C. Lithgow-Bertelloni (2011), Thermodynamics of mantle minerals–II. Phase equilibria, *Geophys. J. Int.*, *184*, 1180–1213, doi:10.1111/j.1365-246X.2010.04890.x.

Sun, D., and D. Helmberger (2008), Lower mantle tomography and phase change mapping, *J. Geophys. Res.*, *113*, B10305, doi:10.1029/2007JB005289.

Tackley, P. J. (2007), Mantle geochemical geodynamics, in *Treatise on Geophysics*, vol. 7, *Mantle Dynamics*, edited by D. Bercovici and G. Schubert, pp. 437–505, Elsevier, Boston, Mass.

Tackley, P. J. (2011), Living dead slabs in 3-D: The dynamics of compositionally stratified slabs entering a 'slab graveyard' above the core-mantle boundary, *Phys. Earth Planet. Inter.*, *188*, 150–162, doi:10.1016/j.pepi.2011.04.013.

Tackley, P. J. (2012), Dynamics and evolution of the deep mantle resulting from thermal, chemical, phase and melting effects, *Earth Sci. Rev.*, *110*, 1–25, doi:10.1016/j.earscirev.2011.10.001.

Tackley, P. J., T. Nakagawa, and J. W. Hernlund (2007), Influence of the post-perovskite transition on thermal and thermochemical mantle convection, in *Post-Perovskite: The Last Mantle Phase Transition*, *Geophys. Monogr. Ser.*, vol. 174, edited by K. Hirose et al., pp. 229–247, AGU, Washington, D. C., doi:10.1029/174GM16.

Tateno, S., K. Hirose, N. Sata, and Y. Ohishi (2009), Determination of post-perovskite phase transition boundary up to 4400 K and implications for thermal structure in D″ layer, *Earth Planet. Sci. Lett.*, *277*, 130–136, doi:10.1016/j.epsl.2008.10.004.

Thomas, C., J.-M. Kendall, and J. Lowman (2004), Lower-mantle seismic discontinuities and the thermal morphology of subducted slabs, *Earth Planet. Sci. Lett.*, *225*, 105–113.

Thorne, M. S., and E. J. Garnero (2004), Inferences of ultralow-velocity zone structure from a global analysis of *SPdKS* waves, *J. Geophys. Res.*, *109*, B08301, doi:10.1029/2004JB003010.

Trampert, J., P. Vacher, and N. Vlaar (2001), Sensitivities of seismic velocities to temperature, pressure and composition in the lower mantle, *Phys. Earth Planet. Inter.*, *124*, 255–267, doi:10.1016/S0031-9201(01)00201-1.

Trampert, J., F. Deschamps, J. Resovsky, and D. A. Yuen (2004), Probabilistic tomography maps chemical heterogeneities throughout the lower mantle, *Science*, *306*, 853–856, doi:10.1126/science.1101996.

Tsuchiya, T., J. Tsuchiya, K. Umemoto, and R. M. Wentzcovitch (2004), Elasticity of post-perovskite $MgSiO_3$, *Geophys. Res. Lett.*, *31*, L14603, doi:10.1029/2004GL020278.

van der Hilst, R. D., W. V. de Hoop, P. Wang, S.-H. Shim, P. Ma, and L. Tenorio (2007), Seismostratigraphy and thermal structure of Earth's core-mantle boundary region, *Science*, *315*, 1813–1817, doi:10.1126/science.1137867.

Williams, Q., and E. J. Garnero (1996), Seismic evidence for partial melt at the base of Earth's mantle, *Science*, *273*, 1528–1530, doi:10.1126/science.273.5281.1528.

Wookey, J., S. Stackhouse, J.-M. Kendall, J. Brodholt, and G. D. Price (2005), Efficacy of the post-perovskite phase as an explanation for lowermost-mantle seismic properties, *Nature*, *438*, 1004–1007, doi:10.1038/nature04345.

Xu, W., C. Lithgow-Bertelloni, L. Stixrude, and J. Ritsema (2008), The effect of bulk composition and temperature on mantle seismic structure, *Earth Planet. Sci. Lett.*, *275*, 70–79, doi:10.1016/j.epsl.2008.08.012.